https://doi.org/10.5194/acp-2022-94
Preprint. Discussion started: 7 April 2022
© Author(s) 2022. CC BY 4.0 License.

Atmospheric Chemistry and Physics Discussions

Modelling coarse and giant desert dust particles

Eleni Drakaki[1,2], Vassilis Amiridis[1], Alexandra Tsekeri[1], Antonis Gkikas[1], Emmanouil Proestakis[1], Sotirios Mallios[1], Stavros Solomos[3], Christos Spyrou[1], Eleni Marinou[1,4], Claire L. Ryder[5], Demetri Bouris[6], and Petros Katsafados[2]

[1]IAASARS, National Observatory of Athens, Athens GR-15236, Greece
[2]Harokopion University of Athens (HUA), Department of Geography, Athens GR-17671, Greece
[3]Academy of Athens, Research Centre for Atmospheric Physics and Climatology, Athens GR-10679, Greece
[4]Institut für Physik der Atmosphäre, Deutsches Zentrum für Luft- und Raumfahrt, Oberpfaffenhofen, Germany
[5]University of Reading, Department of Meteorology, Reading, RG6 6BB, UK
[6]National Technical University of Athens, School of Mechanical Engineering, Athens, GR-15780, Greece

Correspondence to: Eleni Drakaki (eldrakaki@noa.gr)

Abstract. Dust particles larger than 20 μm in diameter (0.2 μm < D < 100 μm) have been regularly observed to remain airborne during long-range transport. In this work we extend the parameterization of mineral dust cycle in the GOCART-AFWA dust scheme of WRFV4.2.1, to include also such coarse and giant particles. The initial particle size distribution in our parameterization is based on observations over desert dust sources and the Stokes' drag coefficient has also been updated to account for dust particles of all sizes ($Re < 10^5$). The new code is applied to simulate dust transport over Cape Verde during the August 2015 AER -D campaign. Model results are evaluated using both airborne dust measurements and the CALIPSO-LIVAS pure dust product. The results show that the modeled lifetimes of the coarser particles are shorter than those observed. Various processes are proposed to explain such inaccuracies, such as the electric field inside dust plumes and non-spherical aerodynamics. Additional sensitivity runs are performed by artificially reducing the settling velocities of the particles to compensate for such underrepresented processes in the model. Our simulations show that particles with diameters of 5-17 μm and 40-100 μm are better represented assuming 80% reduction in settling velocity (UR80) while particles at the range 17-40 μm are better represented in the UR60 scenario. The overall statistical analysis shows that the UR80 experiment presents the closest agreement with the airborne in situ measurements both in Cape Verde and over the sources. The UR80 experiment improves also the vertical distribution of dust in the model, as compared to the CALIPSO-LIVAS pure dust product. Further research is requested in order to understand the physical processes behind the reduction of settling velocity.

1 Introduction

Dust is the prominent contributor to the aerosol burden worldwide and ranks second in aerosol emissions (Textor et al., 2006). The major sources of dust span the "dust belt" (Prospero et al., 2002) in the Northern Hemisphere, which hosts deserts, bare,

https://doi.org/10.5194/acp-2022-94
Preprint. Discussion started: 7 April 2022
© Author(s) 2022. CC BY 4.0 License.

and erodible soils (e.g.,Goudie and Middleton, 2006), that are prone to windblown dust emissions. Most of the global dust budget comes from the Sahara Desert, followed by deserts in the Middle East and Asia. (Ginoux et al., 2012; Huneeus et al., 2011; Kok et al., 2021; Li and Osada, 2007). Spatially limited desert regions in the Southern Hemisphere emit lower amounts of mineral particulate matter (Ginoux et al., 2012; Huneeus et al., 2011; Kok et al., 2021; Li and Osada, 2007) , and less than 5% comes from high-latitude sources (Bullard et al., 2016).

Dust particles act as ice nuclei (IN) on cold cloud processes (Marinou et al., 2019; Solomos et al., 2011) and when mixed or coated with hygroscopic material, they can affect warm cloud processes (Twohy et al., 2009) and serve as cloud condensation nuclei (CCN). Dust particles rich in key micronutrients such as iron (Fe) and phosphorus (P) affect biogeochemical processes in marine and terrestrial ecosystems (Jickells et al., 2005; Okin et al., 2004; Stockdale et al., 2016; Tagliabue et al., 2017) and disrupt the carbon cycle (Jickells et al., 2014) during their wet and dry deposition. Severe dust episodes can affect aviation and telecommunications (Harb et al., 2013; Weinzierl et al., 2012; Nickovic et al., 2021), human health (e.g., Du et al., 2016; Giannadaki et al., 2014) and solar power generation (Kosmopoulos et al., 2018).

In addition to the intensity of dust load, a key factor in the effects of dust particles on weather and climate is the size of the suspended mineral particles. Larger dust particles act more effectively as CCN (Petters and Kreidenweis, 2013) and IN (Diehl et al., 2014) altering cloud microphysical processes, their evolution and dissolution, and subsequently the hydrological cycle in the atmosphere. Recent research suggests that coarser dust aerosols are more effective at absorbing incoming solar radiation, thus enhancing atmospheric warming (Mahowald et al., 2014; Ryder et al., 2019). A complete representation of the dust particle size distribution (PSD) is required for the comprehensive study of dust-related processes in the atmosphere and the assessment of associated impacts.

The diameter (D) range of airborne dust particles is mainly between 0.2 μm and 300 μm, while even larger particles with diameters up to 450 μm have been reported from in situ deposition measurements from buoys in the Atlantic Ocean (van der Does et al., 2018). The size range of particles is usually divided into three different modes, fine, coarse, and giant, without strictly defined limits (Goudie, 2014; Knippertz and Stuut, 2014). According to Ryder et al. (2019), the fine mode includes dust particles with $D \leq 2$ μm, for the coarse mode 2μm $< D <$ 20 μm, and for the giant mode $D \geq 20$ μm. A recent study (Ryder et al., in preparation) suggests that the above modes can be further divided into four categories, namely fine ($D <$ 2.5 μm), coarse (2.5-10 μm), super-coarse (10-62.5 μm), and giant ($D >$ 62.5 μm).

The existence of dust particles larger than 20 μm in diameter was already demonstrated in the 1970s based on measurements in the Caribbean (Prospero et al., 1970). Nevertheless, these sizes were neglected in atmospheric dust models because such particles were assumed to be rare. This assumption has been disproved in recent decades by a large number of airborne campaigns equipped with state-of-the-art in situ and remote sensing instruments. Specifically, SAMUM1 (Weinzierl et al., 2009) and SAMUM2 (Liu et al., 2018) experimental campaigns took place over dust sources and downwind areas (i.e., off the western coasts of N. Africa), in 2006 and 2011 respectively, and presented that over the sources dust aerosols up to 40 μm in diameter were recorded in 20% of the identified dust layers, while over Cape Verde mineral particles up to 30 μm in diameter were measured (Weinzierl et al., 2011), which indicate a reduction in dust particle size along the transport path due to gravity

https://doi.org/10.5194/acp-2022-94
Preprint. Discussion started: 7 April 2022
© Author(s) 2022. CC BY 4.0 License.

settling. Similar results were reported in the FENNEC campaign (Ryder et al., 2013b) with mean effective particle diameters of 22 to 28 μm and 15 to 18 μm for fresh and aged dust, respectively. During the AER-D campaign in Saharan outflow areas near Cape Verde and the Canary Islands, mineral particles with diameters greater than 20 μm were systematically recorded, while their diameters exceeded 40 μm in 36% of the total cases (Ryder et al., 2018a); Dust particles with diameters of 10 to 30 μm were detected during the SALTRACE campaign in Barbados (Weinzierl et al., 2017a), showing that they occur at larger distances than would be expected according to Stokes' theory of gravity.

Atmospheric dust models are the optimal tool to represent the components of the dust cycle and to study the dust-related effects. However, the state-of-the-art atmospheric dust models are characterized by inherent limitations in accounting for realistic dust size distribution in emission and transport (Huang et al., 2020; Kok, 2010; Mahowald et al., 2014). To overcome these drawbacks, we need to include the giant particles in the models in order to study the processes that keep the larger dust aerosols in the atmosphere for longer periods than expected.

Ginoux, (2003) modeled dust aerosols up to 70 μm in diameter using the Global Ozone Chemistry Aerosol Radiation and Transport (GOCART) model and examined the effects of nonsphericity assuming randomly oriented ellipsoidal particles. His results showed that reducing the settling velocity efficiently reproduces the observations when the aspect ratio is equal or greater than 5. The new modeled particle size distributions (PSDs) were in generally better agreement with the AERONET observations, although the PSDs were significantly underestimated for diameters near 10 μm. The aspect ratio of 5 results in a reduction in settling velocity of about 45% for particles with sphere volume-equivalent diameters near 10 μm and 60% for particles with sphere-volume-equivalent diameters near 30 μm. Maring et al. (2003) applied a simple empirical model and suggested that an upward velocity of 0.0033 ms^{-1} (0.33 cm s^{-1}) is required to accurately predict PSD changes during transport. Although their comparisons were limited to sizes up to 25 μm, they pointed out that unknown or not well-known processes counteract settling by gravity. Proposed mechanisms include: (i) vertical mixing within the Saharan air layer during the day (Gasteiger et al., 2017), (ii) the lower settling velocities of non-spherical dust particles (Huang et al., 2020; Mallios et al., 2020), (iii) the underrepresented meteorological conditions (O'Sullivan et al., 2020), (iv) the unresolved turbulence (Gu et al., 2021), (v) the electrification of dust (Daskalopoulou et al., 2021; Mallios et al., 2021; Joseph R. Toth III et al., 2020; Renard et al., 2018; Nicoll et al., 2011) and (vi) the numerical errors that perturb the mass balance (Ginoux, 2003a).

In this work, we demonstrate for the first time a method for incorporating coarse and giant desert dust particles (D > 20 μm, according to the definition of dust modes in Ryder et. al, (2019) into the Advanced Research Weather version of the Weather Research and Forecasting (WRF-ARW) model in conjunction with the GOCART (Ginoux et al., 2001) aerosol model and the Air Force Weather Agency (AFWA) dust emission scheme (LeGrand et al., 2019) (WRF-GOCART-AFWA model). We use advanced in situ measurements from PSD to initialize the model. To evaluate our results, we use both in situ measurements of PSD and satellite retrievals of the extinction coefficient and compare the modelled PSDs after transport and the vertical distribution of dust layers. In addition, we reduce the settling velocity of the particles in the model and study the effects on the dust field properties.

https://doi.org/10.5194/acp-2022-94
Preprint. Discussion started: 7 April 2022
© Author(s) 2022. CC BY 4.0 License.

The article is organized as follows: In Sect. 2, we describe the methodology in terms of the changes we made to the code of WRF-GOCART-AFWA, the setup of the model and the experiments performed, and the observational data we used for model validation. The results of our work are presented in Sect. 3 and Sect. 4 contains the discussion and conclusions of this work.

2 Model and Data

2.1. WRF-GOCART-AFWA model

In our numerical experiments to study the transport of coarse and giant dust aerosols, we use the WRF-ARWv4.2.1 model coupled with the GOCART aerosol model and the AFWA dust emission scheme (LeGrand et al., 2019). The current version of the WRF-GOCART-AFWA model accounts for giant dust particles in the calculated dust emission fluxes (up to 125 μm) and assumes that the transported dust particles are up to 20μm in diameter. To extend the transport PSD to coarser and giant mineral particles, we implemented several developments in the standard WRF-GOCART-AFWA model, which are described and discussed in Sect. 2.1.1 and 2.1.2. Figure 1 shows a sketch of the workflow: the first three steps refer to the implemented extensions in the standard WRF-GOCART-AFWA code: In **step 1**, we establish the definition of a prescribed PSD for the emitted dust particles at the source based on in situ reference measurements, and we distribute the total emitted dust accordingly; in **step 2**, we define five size ranges (five model size bins) for the transported PSD to cover the entire size range of dust particles in the atmosphere (Sect. 2.1.1); in **step 3**, we implement an updated drag coefficient that applies to the sizes of the entire range of Aeolian dust PSD (Sect. 2.1.2). These code changes are integrated into the new WRF-L model. Table 1 shows the properties of the size bins in the standard WRF-GOCART-AFWA code and the size classes defined in the new WRF-L code. The final **step 4** is to perform model experiments and validate the model results using different model configurations against observations (Sect. 2.2), as described in detail in Sect. 3.

2.1.1 Dust size distribution

In observational studies of non-spherical particles, it is customary to describe their size in terms of spherical volume equivalent diameter. In the following, particle size data refer to sphere volume-equivalent diameter, unless otherwise noted. To describe the size of the particles in the size bins of the WRF-L model, we use the sphere-volume-equivalent effective diameter (D_{eff}), which is more relevant to the optical properties of the particles (Hansen and Travis, 1974). In this way, we simplify the comparison between the model calculations and the observations of the optical properties of the particles (e.g., dust optical depth). The D_{eff} of each size bin is calculated as shown in Eq. 1, and is provided in Table 1.

$$D_{eff} = \frac{\int_{D_{lo,k}}^{D_{u,k}} D^3 \cdot \frac{dN}{dD} \cdot dD}{\int_{D_{lo,k}}^{D_{u,k}} D^2 \cdot \frac{dN}{dD} \cdot dD}, \quad (1)$$

https://doi.org/10.5194/acp-2022-94
Preprint. Discussion started: 7 April 2022
© Author(s) 2022. CC BY 4.0 License.

Where D is the particle diameter in (μm) and $\frac{dN}{dD}$ is the particle number size distribution in number of particles per cm^{-3}. The parameters of each size bin i are shown in Table 3. Henceforward, references about the size of the particle correspond to particle volume equivalent diameter, unless mentioned otherwise.

In the default GOCART-AFWA of WRF, the total emitted vertical dust flux is estimated at each grid point prone to dust emission, when favorable conditions are met. The dust flux is then distributed over five transport size bins, based on the fragmentation theory of Kok, (2011), although limited to diameters up to 20 μm. Since our goal is to include larger dust particles than those commonly used in current atmospheric dust models, we redefine the five transport model bins to include particles with diameters up to 100 μm (Table 1). We use a prescribed PSD for emitted dust particles at the source based on in situ measurements from the FENNEC campaign (Ryder et al., 2013a). Ryder et al., (2013a) made airborne in situ measurements of dust PSDs at various altitudes near dust sources in the Sahara Desert. The emitted dust PSD used in our work is derived from measurements of fresh upwelling cases at the lowest available altitudes from aircraft profiles representative of 1 km and is hereafter referred to as the "observed FENNEC-PSD". The observed FENNEC-PSD is shown in Fig. 2(a) with red squares, and the shaded areas show the size range of the individual bins. In Sect. 2.2.1 more information are provided about the FENNEC campaign and the instruments used for the measurements.

The distribution of emitted mass over the redefined size range is obtained by calculating the mass fraction resulting from the weighting factors ($k_{factors}$) for each transport bin, as shown in Eq. 2. The weighting factors are also shown in Fig.2(b).

$$k_{factors} = \int_{Dlo,k}^{Du,k} \frac{1}{D} \cdot \frac{dV}{dlnD} \cdot dD, \quad (2)$$

Where D is the particle diameter, $\frac{dV}{dlnD}$ is the volume size distribution in μm^{3}cm^{-3}, $D_{lo,k}$ and $D_{u,k}$ are the margins of each size bin k in μm.

2.1.2 Updated gravitational scheme

In WRF-GOCART-AFWA, the forces acting on a dust particle moving along the vertical direction, are the gravitational force F_g and the aerodynamic drag force F_{drag}, which are mathematically expressed in Eq.3 and Eq.4, respectively.

$$F_g = \rho_p \cdot V_p \cdot g, \quad (3)$$

$$F_{drag} = \frac{1}{2} \cdot \frac{C_D}{C_{cun}} \cdot A_p \cdot \rho_{air} \cdot u_{term}^2, \quad (4)$$

The constant velocity that a particle builds up, as it falls vertically in the Earth's atmosphere, is defined as the terminal settling velocity u_{term}, and it can be estimated by solving the 1-D equation of motion in the steady state limit, where ΣF is assumed to be equal to zero:

https://doi.org/10.5194/acp-2022-94
Preprint. Discussion started: 7 April 2022
© Author(s) 2022. CC BY 4.0 License.

$$\rho_p \cdot V_p . g = \frac{1}{2} \cdot C_D \cdot A_p \cdot \rho_{air} . u_{term}^2, \quad (5)$$

Where ρ_p is the particle density in $\frac{kg}{m^3}$, g is the gravitational acceleration in $\frac{m}{s^2}$, V_p is the particle volume in m^3 and A_p is the particle projected area normal to the flow in m^2, ρ_{air} is the atmospheric air density in $\frac{kg}{m^3}$ and C_D is the aerodynamic drag coefficient (unit less). For each size bin it is assumed that the particles are spherical with diameter D_{eff} in m (as defined in Sect. 2.1.1), thus their volume and projected area are defined by the following equations for spheres:

$$A_p = \frac{\pi}{4} \cdot D_{eff}^2, \quad (6)$$

$$V_p = \frac{1}{6} \cdot \pi \cdot D_{eff}^3, \quad (7)$$

The drag coefficient is that of Stokes' Law and is defined as:

$$C_D = \frac{12}{Re}, \quad (8)$$

Where Re is the Reynold's number (unit less) given by the following equation:

$$Re = \frac{\rho_{air} \cdot u_{term} \cdot D_{eff}}{2 \cdot \mu}, \quad (9)$$

Where μ is the air dynamic viscosity in $\frac{kg \cdot s}{m}$ defined as a function of air temperature T in ^oK by the following equation:

$$\mu = \frac{1.4.58 \cdot 10^{-6} \cdot T^{\frac{3}{2}}}{T + 110.4}, \quad (10)$$

Equation 7 has been derived with the simplification of no-slip boundary conditions, thus a correction factor C_{cun}, proposed by Davies, C. N. (1945), is applied to the Stokes' relationship to account for velocity slip at the particle's surface. The corrected drag coefficient become is:

$$C_{D,slip} = \frac{C_D}{C_{cun}}, \quad (11)$$

Where C_{cun} is given by:

https://doi.org/10.5194/acp-2022-94
Preprint. Discussion started: 7 April 2022
© Author(s) 2022. CC BY 4.0 License.

$$C_{cun} = C_{cun}(\lambda) = 1.0 + \frac{2\cdot\lambda}{D_{eff}}[1.257 + 0.4 \cdot e^{\frac{-1.1\cdot D_{eff}}{2\cdot\lambda}}], \quad (12)$$

Where $\lambda = \frac{1.1\cdot 10^{-3}\cdot\sqrt{T}}{P}$ is the air mean free path in m and μ is the air dynamic viscosity in $\frac{kg\cdot s}{m}$, as defined by Eq.10. T is the air temperature in ^{o}K and P the air pressure in hPa.

Substituting Eq. 6-9 in Eq. 4 we end up with the relationship for the terminal velocity of the dust particles, as shown in Eq. 12.

$$u_{term} = \frac{\rho_p \cdot g \cdot D_{eff}^2 \cdot C_{cun}}{18 \cdot \mu}, \quad (13)$$

The slip-corrected drag coefficient of the Stokes' Law (Eq.10) is valid only when Re <<1, thus it is not representative for particles with D_{eff} larger than ~10 μm. Since our work includes dust particles with diameters larger than 20 μm, the drag coefficient must be representative for higher values of Re (i.e., $0 < Re < 16$). For this reason, we adapt the drag coefficient C'_D of Eq.13, proposed by (Clift and Gauvin, 1971), instead. C'_D has been recently used in (Mallios et al., 2020) as a reference for the development of a drag coefficient for prolate ellipsoids, as more valid for $Re < 10^5$ (Clift et al., 2005).

$$C'_D = \frac{12}{Re} \cdot (1 + 0.2415 \cdot Re^{0.687}) + \frac{0.42}{1+\frac{19019}{Re^{1.16}}}, \; for \;\; Re < 10^5 \quad (14)$$

Using Eq.5, 6, 7, 9 and 14 we calculate the terminal velocity for each model size bin. Since the resulting equation is not linearly dependent by D_{eff} we apply the bisection method to solve the equation.

In the default code the slip correction is applied unconditionally, as mentioned above, for all the values of Re. However, slip correction is defined in Stokes' regime (Mallios et al., 2020). Thus, in the updated drag coefficient, only when Re < 0.1 (Stokes' regime), we recalculated the settling velocity using the corrected drag coefficient $C_{d.slip} = C'_D / C'_{cun}$, where $C'_{cun} = C_{cun}(\lambda')$ with λ' the mean free path adopted by (Jennings, 1988):

$$\lambda' = \sqrt{\frac{\pi}{8}} \cdot \frac{\frac{\mu}{0.4987445}}{\sqrt{P\rho_{air}}}, \quad (15)$$

here μ is air dynamic viscosity in $\frac{kg\cdot s}{m}$, as defined by Eq.10, and the atmospheric pressure P is in Pa.

2.1.3 Model experiments

Using the WRF-L code, we run a simulation that serves as a CONTROL experiment. Our simulation period coincides with the AER-D experimental campaign and covers the days from July 29, 2015 to August 25, 2015 for a region extending in latitude

https://doi.org/10.5194/acp-2022-94
Preprint. Discussion started: 7 April 2022
© Author(s) 2022. CC BY 4.0 License.

and longitude along [1.42ºN;39.99ºN] and [46.87ºE;30.87ºW] (Fig. 3). The simulation area is located over the major Saharan sources and also includes the downwind areas in the eastern sector of the tropical Atlantic. We use an equal-distance grid with a spatial grid spacing of 15 km x 15 km that includes 550 × 300 points and 70 vertical sigma pressure levels up to 50 hPa. For each run, 84-hour forecast cycles are performed and reinitialized every 3 days using the 6-hour Global Forecast System Final Analysis (GFS - FNL) reanalysis product, available at a 0.25ºx0.25º model grid, to initialize the model and set boundary conditions. The first week of the simulation served as a spin-up run for the accumulation of the background dust loading and is excluded from the analysis. The simulation run in a dust-only mode, without including radiative feedback from aerosols, to avoid (in this first case) a more complicated analysis that would include the radiative effect on dust transport. The scaling of the dust source strength is chosen to best match the modeled DOD with the AERONET measurements (RMSE=0.34, bias=-0.07) from the desert stations: Banizoumbou, Dakar, El_Farafra, Medenine- IRA, Oujda , Tizi_Ouzou, Tunis_Carthage ,Ben_Salem). We only use the measurements where DOD is higher than 0.75 and the Angstrom exponent is lower than 0.2 to ensure that contamination by aerosols other than dust is negligible. The complete configuration options for the run are listed in Table 2.

In addition, we investigate the implications of a possible mechanism to counteract gravitational settling in order to reduce the differences between the CONTROL run calculations and the in situ observations (shown in Sect. 3.4). To this end, we perform additional sensitivity tests by reducing the settling velocity by 20 to 80%, with a step size of 20%. The experiments are referred to as the "URx experiment", using the percentage (x%) by which the settling velocity is reduced. With this artificial tuning, we aim to reproduce the net force acting on dust particles falling into the atmosphere and overcome the current shortcomings of the model (i.e., the absence of all real forces that determine the lifetime of dust particles in nature).

It should be noted that several studies have pointed out the importance of fine-resolution dust simulations (Solomos et al., 2012; Basart et al., 2016; Gu et al., 2021;), which, among other things, help the model resolve small-scale dynamics and account for possible interactions between different scales. Given the complicated meteorological conditions during the study period (i.e., August 2015), the fine resolution increases the accuracy of the dust simulations and provides a good estimate of the magnitude of the missing mechanism. The reduced deposition of particles can be attributed to either an updraft counteracting gravity or a reduction in particle settling velocity, both of which slow dust deposition rates. In the first case, this can be attributed to either as yet unresolved meteorological conditions (e.g., small-scale haboobs, dunes) or atmospheric feedbacks due to dust-radiation interactions (i.e., atmospheric heating due to absorption of solar radiation by mineral particles). Lower settling velocities may be related to higher aerodynamic forces due to the non-spherical shape and orientation of dust particles (Ginoux, 2003b; Loth, 2008; Zastawny et al., 2012; Shao et al., 2017; Sanjeevi et al., 2018; Mallios et al., 2020;), or upward electric forces acting on dust particles (Ulanowski et al., 2007; Daskalopoulou et al., 2021; Mallios et al., 2021;). The full list of experiments performed can be found in Table 3.

https://doi.org/10.5194/acp-2022-94
Preprint. Discussion started: 7 April 2022
© Author(s) 2022. CC BY 4.0 License.

2.1.4 Dust extinction coefficient and dust optical depth

In Sect. 3.5, we compare the model calculations of dust extinction at 550 nm with the product of the pure dust extinction coefficient from the LIdar climatology of Vertical Aerosol Structure for space-based lidar simulation studies (LIVAS). To this end, we first project the two data sets (model and LIVAS) onto a common horizontal grid. We thus convert the 15-km horizontal grid of the model output to a 1°x1°-degree grid to match the ~111km horizontal grid of LIVAS. The model extinction coefficient for each size bin k ($EC_{550,k,n,l}$) is then calculated for each horizontal grid box n and for each model level l, as shown in Eq.16.

$$EC_{550,k,l,n} = \sum_1^k \frac{3}{2\rho_{,k} D_{eff,k}} M_{n,k,l} Q_{ext550,k}, \tag{16}$$

where $M_{n,k,l}$, ρ_n and $D_{eff,k}$ are the dust mass concentration in g/m^3, the particle density in g/cm^3, and the effective diameter in μm of size bin k. $Q_{ext550,k}$ is the extinction efficiency at 550 nm, calculated using the Mie scattering code (Mie, 1908), considering a spherical shape for the dust particles, and a refractive index of 1.55 + i0.005, which is representative of dust (e.g. Dubovik et al., 2002). For simplification of the computations, we assume that the particles in each size bin have the same size (i.e. $D_{eff,k}$), and thus the same $Q_{ext550,k}$. Along the vertical direction, the LIVAS dataset is collocated to the coarser model grid, by averaging across the margins of each model vertical grid box.

The DOD at 550 nm is computed for every horizontal grid box n of the model, as shown in Eq. 17. For the evaluation of the calculated DOD, we use the ModIs Dust AeroSol (MIDAS) DOD product (see Sect. 2.2.3), after applying the following spatiotemporal collocation: First, the calculated DODs are re-projected on an equal lat-lon grid, with 0.4° x 0.4° grid. The DOD is provided by WRF on an hourly basis without spatial gaps, in contrast to MIDAS DOD, which is available at swath level with a viewing width of 2330 km, along the MODIS-Aqua polar orbit, at 5-minute segments (see Gkikas et al., 2021) for further details). The MIDAS swaths are re-projected on the horizontal grid of the WRF, with 0.4° x 0.4° grid spacing. Then, the WRF outputs that are closer to the Aqua satellite overpass time, are used to calculate a weighted-average WRF DOD, only for WRF grid cells with coincident MIDAS DODs, by taking into account the absolute difference between WRF forecast time and Aqua overpass time.

$$DOD_{550,n} = \sum_1^k \frac{3}{2\rho_{,k} D_{eff,k}} M_{n,k} Q_{ext550,k}, \tag{17}$$

2.2 Observational datasets

2.2.1 Airborne in situ observations

The airborne in situ measurements used in this study, were collected during the FENNEC and the AER-D campaigns. Both campaigns employed the FAAM BAE 146 research aircraft, equipped with similar instrumentation for measurements of the

https://doi.org/10.5194/acp-2022-94
Preprint. Discussion started: 7 April 2022
© Author(s) 2022. CC BY 4.0 License.

dust PSD. During the FENNEC campaign the flights were performed above the Sahara dust sources, above Mauritania and West Mali, while during the AER-D campaign the flights were performed away from the dust sources, in the vicinity of Cape Verde and Canary Islands. The trajectories of AER-D flights and the approximate locations of each run (i.e. near-horizontal flight segment) are depicted in Fig.3. The suite of airborne in situ instruments included the Passive Cavity Aerosol Spectrometer Probe (PCASP) and the Cloud Droplet Probe (CDP), alongside with either the Cloud-Imaging Probe 15 (CIP15), or the 2-D Stereo probe (2DS). During the FENNEC campaign, the measurements provided PSD data for diameters up to 300μm, while during the AER-D campaign, the PSD was provided for particles with diameters up to 200μm. Full details of instrumental measurements and processing are given by Ryder et al., (2013b) and Ryder et al., (2018), for FENNEC and AER-D, respectively. In Sect. 2.1.1 we describe the way that FENNEC campaign measurement used in this study.

2.2.2 LIVAS product

For the validation of the vertical distribution of dust from the model (see Sect. 3.5), we utilize the pure-dust profiles provided by the LIVAS dataset, originally presented in Amiridis et al. (2013; 2015) and updated in Marinou et al. (2017). The LIVAS pure-dust product is a global dataset, covering the period between 06/2006 and 05/2020, and is provided a) on per-granule level with similar resolution to the original Cloud-Aerosol Lidar and Infrared Pathfinder Satellite Observations (CALIPSO) L2 profile products (i.e., 5 km horizontal and 60 m vertical), and b) as a global three-dimensional database of monthly-mean averaged profiles of aerosol properties, on a uniform horizontal grid spacing of 1° × 1°. LIVAS was developed applying the dust-separation technique described in Tesche et al., (2009) on the CALIPSO level 2 version 4 products (Winker et al., 2009). The LIVAS pure-dust product has been used to a variety of dust-oriented studies including the investigation of the dust sources and the seasonal transition of the dust transport pathways (Marinou et al., 2017; Proestakis et al., 2018); the evaluation of the performance of atmospheric and dust transport models (e.g. Tsikerdekis et al., 2017; Solomos et al. 2017; Georgoulias et al., 2018; Konsta et al., 2018), the evaluation of new satellite-based products (e.g. Georgoulias et al., 2016; Chimot at al. 2017; Georgoulias et al., 2020; Gkikas et al., 2021), and on dust assimilation experiments (Escribano et al., 2021). Herein, the LIVAS pure-dust extinction product is used for the assessment of the simulated dust vertical patterns. In the geographical region of our study, the uncertainty of the product is estimated to be less than 20% in altitudes up to 6km (Marinou et al. 2017).

2.2.3 MIDAS product

For the assessment of the simulated horizontal dust patterns (see Sect. 3.2), the recently-developed MIDAS dataset (Gkikas et al., 2021) has been utilized. MIDAS has been produced via the synergy of the quality-filtered MODIS aerosol optical depth (AOD, Collection 6.1, Level 2) and the fraction of AOD attributed to dust (MDF), provided by the Modern-Era Retrospective Analysis for Research and Applications (MERRA-2 version 2; Gelaro et al., 2017). According to the applied methodology, the columnar DOD at 550 nm is derived at fine spatial grid spacing (0.1° x 0.1°), along with its associated uncertainty (see Sect. 3 in Gkikas et al., (2021)). MIDAS DOD has been evaluated versus AERONET AOD retrievals (Giles et al., 2019), in which the contribution of non-dust aerosol species has been minimized. In the region of interest of the current study (i.e., West

https://doi.org/10.5194/acp-2022-94
Preprint. Discussion started: 7 April 2022
© Author(s) 2022. CC BY 4.0 License.

Sahara and eastern Tropical Atlantic Ocean), MIDAS DODs covariate (R ~0.90) very well with AERONET-derived DODs, although they are slightly overestimated by <0.04 (see Fig. 4 in Gkikas et al., (2021)). Moreover, the intercomparison of MIDAS, LIVAS and MERRA-2 DODs show a remarkable consistency in reproducing the seasonal cycle of dust loads over the W. Sahara and the eastern segment of the Tropical Atlantic Ocean. Overall, the MIDAS dataset is quite useful for the current study, due to the high reliability of the derived DOD product and the product availability at fine spatial resolution, on a daily basis.

2.2.4 MSG-SEVIRI-DUST RGB product

We use the Meteosat Second Generation - Spinning Enhanced Infrared and Visible Imager (MSG-SEVIRI) DUST RGB product, which is produced by the RGB colors (Red-Green-Blue), corresponding to the three infrared channels of the MSG-SEVIRI instrument. The functionality of the geostationary SEVIRI sensor in the infrared area of the electromagnetic spectrum, and the combination of the different sensitivities of the three channels, enables both daytime and nighttime continuous observations, along with the discrimination between land, clouds and aerosols, making the Dust RGB product very useful for monitoring intense dust and volcanic ash plumes. Dust particles are depicted on images as bright magenta (during day) or purple color (during night) over land, and as a magenta color over the sea.

3 Results

3.1 Settling Velocities

Figure 4 shows the altitude profiles of the settling velocities for each size bin from the CONTROL run, averaged over the simulation domain, and the simulation period. As the size gets bigger the settling velocity is increased. Terminal velocities of particles of bin 5 are two orders of magnitude greater than the particles of bin 2 and bin 3, and one order of magnitude greater than the particles of bin 4. The terminal velocities increase with height following the temperature lapse rate, and are sensitive to the thermodynamic condition of the atmospheric air, increasing as temperature or air density drops, based on Eq.10, 13 and the relationships of air viscosity. The average settling velocities for the CONTROL run near the surface differ from those at 6 km height, by approximately 10 %, which is a significant reduction, especially for coarser and giant particles where velocities are greater.

3.2 Dust above the sources

Figure 5 shows the change of the dust volume PSD with height above an emission point in Mali, on 12/08/2015, with the dust concentration reducing considerably for heights greater than 2 km. This point is in the area of intense emissions, observed both from satellites and the model. The area of Mali is also suggested by Ryder et al. (2013) as one of the dust sources of the dust plume that measurements of flight b928 were taken. Fig. 5 shows how the concentration of every size bin of the model is reduced with increase in altitude. The reduction is more evident for the particles of bin 4 and bin 5, where the volume

https://doi.org/10.5194/acp-2022-94
Preprint. Discussion started: 7 April 2022
© Author(s) 2022. CC BY 4.0 License.

concentration is reduced over an order of magnitude between 2 and 3 km. Particles of bin 4 and bin 5 are removed very quickly with height and are found in low concentrations at heights up to 4 km in the model simulations (not shown).

A direct comparison between the modelled and the observed PSD for the dust concentration above the sources, cannot be conducted for the AER-D campaign, since the measurements were only performed over the ocean. Figure 5 shows a more qualitative comparison, using the observed FENNEC-PSD at 1km (red squares). The modelled and observed PSD differ. The modelled volume concentrations have larger values for bins 1-3, and lower for bins 4 and 5. The maximum concentration of the modelled PSD is at bin 3, whereas for the observed PSD is at bin 4, suggesting that the model underestimates the concentrations at bins 4 and 5, already from the initial transport stage, near the dust sources. Those differences can be attributed either to an underestimation of the contribution of the coarser particles on the emission, to an overestimation of their loss during transport from the surface to 1 km, or to higher updrafts that remain unresolved in the simulation of this study.

3.3 Mean dust load and spatiotemporal distribution of dust

In order to further demonstrate the distribution of the total dust mass at the different sizes, Fig. 6 shows the simulated fields of the total columnar dust load, along with the corresponding concentrations at each size bin. The simulations in Fig. 6 are performed using the parameters of the CONTROL experiment, and the calculated concentrations are averaged over the period of interest (5-25/8/15). For the first three bins, the spatial patterns of dust load are very similar, showing the dust sources in the Western Sahara, and the advection of the particles towards the Atlantic Ocean. The mass increases from bin1 to bin 3 (5.5 – 17 μm), which has maximum values for the whole size range. Dust particles with diameters between 17 μm and 40 μm (bin 4) are found mainly over land, and are subjected to short-range transport westwards (i.e., off the Moroccan coast). Giant particles (bin 5) are found at very low concentrations (< 0.5 gr m^{-2}), at isolated areas over/near dust sources, probably due to their quick gravitational settling.

The comparison of the model simulations with satellite retrievals shows that, in general, there is a good agreement on the spatiotemporal distribution of dust during the days and times of the AER-D flights. Deviations between the simulations and the observations are found for flight b920, due to a shift of the center of the simulated dust mass towards the south (Fig. 7(a)). Moreover, the observations show that the dust plume traveled towards Morocco and Canary Islands, whereas the model shows that it traveled mainly towards Cape Verde (see Dust RGB image of MSG-SEVIRI, during the time-of-flight b920 in Fig.7(b), and the MODIS DOD and corrected reflectance in Fig. 7(c) and 7(d), respectively). This difference results in an overestimation of the simulated dust mass in the area of South West Africa and West Mauritania, affecting the transport towards the area of flight b920. The main cause for this discrepancy is the difference in the intensity by which the various dust sources in Northern Algeria were activated during the previous days. As it is depicted in Fig. 7(e, f) there are sources in the model that have been strongly activated in circles A and B, although in RGB-Dust MSG-SEVIRI images they are depicted with much less intensity (fewer pink colors). That deficiency of the model could be attributed to various reasons, such as underrepresentation of the meteorological conditions mostly in cases of haboobs (Ryder, 2018a, 2021) which are responsible for the dust erosion, possibly

https://doi.org/10.5194/acp-2022-94
Preprint. Discussion started: 7 April 2022
© Author(s) 2022. CC BY 4.0 License.

due to a not so sophisticated microphysics scheme or missing smaller scale processes. For those reasons, b920 is excluded from the statistical analysis in Sect. 3.4.

3.4 Dust size distribution

The model PSDs are collocated in space and time with the measurements of each flight segment. To extract the model PSDs, after interpolating the model dust concentrations fields to the specific height of the flight run, we average the dust concentrations of the eight neighboring grid points to the grid point with the nearest latitude and longitude of each flight segment. The performance of the model is similar for the flights b924, b932 and b934. Figure 8 shows the comparison of the CONTROL run with the airborne in situ measurements of flight b928. The model adequately reproduces the volume concentration of the particles for bins 1 and 2, although the agreement is better near the surface and above 4 km. The model underestimates the volume concentration of bin 3, with the simulated values to be within the measurement uncertainties. It also underestimates the volume concentrations of bins 4 and 5, as expected, since the underestimation happens also near the sources, as shown in Fig. 5(a). Considering the different experiments for reduced settling velocities (Table 3), we see that the reduction mainly affects the simulations for the coarser particles (bins 3, 4 and 5), with the effect increasing with the size of the particles. The simulated concentrations of giant particles (bin 5) become significant when the reduction in settling velocity is greater than 60%. The comparison of the observed and modelled mean average PSDs in Fig. 9(a) shows that UR60 and UR80 experiments are closer to the observations, with UR80 to better reproduce the observed values of bins 3 and 5, whereas UR60 better reproduces the values of bin 4. This reduction results in settling velocities of ~0.066 m/s for bin 3 (D=5.5-17 μm), ~0.32 m/s for bin 4 (D=17-40 μm) and ~1,88 m/s for bin5 (40-80μm). In general, UR80 simulations of the mean PSD provide the best agreement with the observations. In terms of total volume, the UR80 simulations have the smallest relative difference with the observations for most flights, providing a ~50% improvement in relative difference, as it is depicted in Fig. 9(b). UR80 also provides better agreement with the observed FENNEC-PSD above the dust sources, by shifting the maximum of the PSD to bin 4 (Fig. 5).

3.5 Dust vertical distribution

Figure 10(a) shows the profile of the mean extinction coefficient at 532 nm, provided by the LIVAS pure-dust product (black line), and the profile of the mean extinction coefficients at 550 nm, provided by the CONTROL, UR20, UR40, UR60, and UR80 experiments. This comparison is an initial demonstration of the good initialization and performance of the different model experiments, with respect to capturing the vertical distribution of dust. The intercompared profiles are in good agreement, with the simulations falling well-within the variability of the dust observations, although discrepancies are also present, especially close to the dust sources, in the nighttime boundary layer (Fig.10(b) – region I), and within the upper free Troposphere (Fig. 10(b) – region III). The discrepancies close to the dust sources are attributed to the complex topography, in terms of geographical characteristics (Proestakis et al., 2018), weighting effects, surface returns, and representativeness issues related to the aggregation of CALIPSO L2 profiles to LIVAS 1°x1° grid resolution (Amiridis et al, 2013, Marinou et al., 2017).

https://doi.org/10.5194/acp-2022-94
Preprint. Discussion started: 7 April 2022
© Author(s) 2022. CC BY 4.0 License.

The discrepancies in the upper free Troposphere (above 6 km) are attributed to the presence of tenuous aerosol layers which fall below the CALIOP layer detection threshold. Thus, the assessment of the different model experiments with the LIVAS pure-dust product, is performed in the region between 1.5 km and 6.4 km a.m.s.l. (Fig. 10 – region II).

According to the comparison of observations and simulations of the mean extinction coefficient (Fig. 10(a)), the statistical overall analysis reveals that the UR40 experiment demonstrates a better performance compared to LIVAS, reducing the mean bias close to zero. However, the UR80 experiment provides a more constant (positive) bias with height, which suggests a better distribution of the dust mass in the vertical.

4 Discussion and Conclusions

The frequent presence of large desert dust particles (D>20 μm) far from their sources, is well established by numerous observational studies over the last decade (van der Does et al., 2018; Liu et al., 2018; Ryder et al., 2013b, 2018a, 2019a; Weinzierl et al., 2009, 2011, 2017b). However, the processes that result in the particle retainment in the atmosphere, and subsequently their travel at greater distances than predicted, remains unrevealed. In this study we extend the particle size range acknowledged in WRF-GOCART-AFWA transport code, to include particles with diameters up to 100 μm. The evaluation against airborne in situ observations of the size distribution shows that larger particles, are underestimated, both above their sources and far from them. This suggests that there are atmospheric processes that are not taken into account in the model simulations. We investigate the effect of reducing the settling velocity of the dust particles due to these unknown processes, and we see that for a reduction of 60% and (especially for) 80%, the simulations of the PSD in Cape Verde are improved with respect to the observations. The reduction of 80% results in settling velocity of 0.066 m/s for particles with D<25 μm, which is double than the value reported by Maring et al. (2003) for similar sizes. It should be noted though that Maring et al. (2003) derived this settling velocity using observations that were taken with a five-year difference. Ginoux (2003), has also reported an improvement in model simulations for a reduction in settling velocity of approximately 45% and 60%, for particles with diameters 10 to 30 μm. Though, the differences in the model resolution, the dust scheme and the drag coefficient in Ginoux (2003) compare to this study, could cause the different values of the required corrections in the settling velocities. The difference with the values suggested herein, can mainly be attributed to the different drag coefficient used in Ginoux (2003), which results in lower settling velocities for the spherical particles.

One of the processes proposed in the literature to explain the longer atmospheric lifetimes of large mineral dust particles is the particle asphericity. Huang et al. (2020) used globally averaged shape distributions of particle aspect ratio and height to width ratio and provided a correction to the spherical particle settling velocity, which is valid for ellipsoidal particles. According to their empirical expression, there is a 20% reduction of particle settling velocity in the case of ellipsoidal particles compared with their spherical counterparts of the same volume. Among the limitations of their methodology (see Huang et al. 2020), is that it is valid only in the Stokes' regime (Re<<1), which limits the applicability of the study for particles with sizes less than 20 μm, and that the ellipsoidal particles are randomly oriented.

https://doi.org/10.5194/acp-2022-94
Preprint. Discussion started: 7 April 2022
© Author(s) 2022. CC BY 4.0 License.

Mallios et al. (2021a) derived semi-analytical expressions for the mean orientation angle of prolate spheroids moving vertically in the Earth's atmosphere in the presence of electrical and gravitational forces. They found that the random orientation assumption is, in principle, valid only for particles with size (two times the particle major semi-axis) less than 2 μm, reducing even more the applicability of the methodology by Huang et al. (2020). As the size increases, the gravity or the electrical force tend to create sufficient torque to rotate the particle horizontally or vertically with respect to the ground, respectively (depending on the particle net electrical charge and the large-scale atmospheric electric field).

Moreover, Mallios et al. (2020) provided new expressions for the drag coefficient of prolate spheroids that are valid beyond the Stokes' regime (specifically for Re≤100) and that take into account the orientation and the aspect ratio of the particle. They showed that in the case the aspect ratio ranges between 1.4 and 2.4, prolate spheroids fall faster than their spherical counterparts of the same volume. This is attributed to the projected area of the prolate spheroids, which depends strongly on the particle orientation (although on average it is larger for ellipsoids than spheres (Vickers, 1996), the projected area of ellipsoids becomes smaller than the projected area of spheres of the same volume as the particle becomes vertically oriented), and the aerodynamic properties due to the impact of the prolate spheroid shape factors on their drag coefficients. They also showed that when comparing prolate spheroids with spherical particles of the same maximum dimension the conclusions are different. In the case of particles with aspect ratio equal to 1.4, the settling velocity of prolate spheroids is on average 6% (in the case of horizontal orientation) up to 23% (in the case of vertical orientation) less than their spherical counterparts (of the same maximum dimension). As the aspect ratio increases to 2.4, the difference becomes 20% (for horizontal orientation) and 52% (for vertical orientation).

Another process that can influence mineral dust settling has to do with the electrical properties of dust particles. The dust particles are charged in the atmosphere either due to the attachment of atmospheric ions on them (Mallios et al. 2021b) or/and due to collisions, a process known as triboelectric effect (Ette, 1971, Eden and Vonnegut, 1973, Mills, 1977, Jayaratne, 1991). Moreover, there is a large-scale atmospheric electric field, due to the potential difference between the lower part of the Ionosphere and the Earth's surface (Rycroft et al., 2008). The electric field is modified by ion attachment process (Mallios et al. 2021b) or by the charge separation caused by updrafts (Krauss et al., 2003). Therefore, electrical forces are generated that might influence the particle settling process by balancing the gravity or changing the particle orientation. The quantification of the particles electrical properties is still an open question.

Triboelectric effect is able to modify the particles saltation process at the emission sources right above the ground due to the generation of very high values of electric charge caused by the large collision frequency which is a consequence of the wind and the large particle number density (Kok and Renno, 2006, 2008). As the particles are aloft, the collision frequency decreases (Rahman et al., 2008) and the ion attachment process can modify the acquired particle charge, because the electric field of the charged particles tend to attract ions of opposite polarities (Mallios et al., 2021b). It is still unknown if the acquired charge of the particles remains or is neutralized. Toth III et al., (2020) estimated that if the particle net charge persists, then the ambient electric field is sufficient to generate electrical forces that can keep particles suspended at higher elevations and enrich the concentration of larger particles at higher elevations. Mallios et al. (2021) calculated the ion-attachment rates of settling

spherical particles in the radius range of 1-100 μm, and found that the maximum electric force that acts upon the particles is two orders of magnitude smaller than the gravity force, and doesn't significantly influence the particle dynamics. They concluded that a generalized model that includes all the particle charging mechanisms is necessary for the proper study of the dust particle electric properties influence on the settling process.

According to aforementioned studies, the particle ashericity seems to be a strong candidate for the suggested corrections in this work. Vertically oriented prolate spheroids with aspect ratio 2.4 can "experience" a 52% velocity reduction compared to their spherical counterparts of the same maximum size. This difference can increase in the case of tri-axial ellipsoidal particles (Huang et al., 2020), or in the case of more aspherical particles. As the electric field and the particle electrical charge are responsible for the particle vertical orientation, the proper quantification of the particle electrical properties and their incorporation into the WRF-L model constitute the future steps of this work.

Finally, it is worth mentioning that a possible source of error in the gravitational loses simulated by the model, are the numerical errors, such as the numerical diffusion in the advection equation of gravitational settling, since WRF-GOCART-AFWA (and the WRF-L) uses a first-order upwind scheme. In any case, the proposed scheme presented here, provides a tool for the investigation of the physical processes in the transport of coarse and giant particles, along with their impacts on other physical processes in the atmosphere, such as ice nucleation and radiation interactions. The artificial reduction in the settling velocity is not attributed to a known physical mechanism (although results from the past literature reveal some candidates that can give results on the same order of magnitude). Thus, despite the encouraging results, more research is needed towards understanding the physical or numerical processes driving this finding, including the estimation of the impact of non-spherical particles, electricity, the radiation impact on thermodynamics and the disturbance of the mass balance due to the numerical diffusion.

Author Contributions: ED, VA, and AT design the study; ED developed the code and performed the simulations. ED, EP and AG analyzed and plot the data; ED wrote the manuscript draft; VA, AT, AG, EP, SM, CS, SS, EM, CR, DB and PK provided critical feedback and helped shape the research, analysis, and reviewed and edited the manuscript.

Funding: This research was supported by D-TECT (Grant Agreement 725698) funded by the European Research Council (ERC). ED would like to acknowledge funding by Greece and the Stavros Niarhos Foundation (SNF). CLR was funded by NERC grant reference NE/M018288/1. EM was funded by the European Research Council 661 (grant no. 725698, D-TECT) and by a DLR VO-R young investigator group and the Deutscher Akademischer Austauschdienst (grant no. 57370121). AG acknowledges support by the Hellenic Foundation for Research and Innovation (H. F. R. I.) under the "2nd Call for H. F. R. I. Research Projects to support Post-Doctoral Researchers" (project acronym: ATLANTAS, project number: 544). The MIDAS dataset has been developed in the framework of the DUST-GLASS project (grant no. 749461; European Union's Horizon 2020 Research and Innovation program under the Marie Skłodowska-Curie Actions.

Acknowledgements: This work was supported by computational time granted from the National Infrastructures for Research and Technology S.A. (GRNET S.A.) in the National HPC facility - ARIS - under project ID pa210502-TRAP-P. We thank the PANhellenic GEophysical observatory of Antikythera (PANGEA) for providing access to the LIVAS and MIDAS data used in this study and their computational center. The National Centers for Environmental Prediction (NCEP) is gratefully acknowledged for the provision of the Global Forecasting System (GFS) operational analyses and the real time global (RTG) sea surface temperature (SST) analyses. We would like to thank the NASA CALIPSO team and NASA/LaRC/ASDC for making the CALIPSO products available, which have been used to build the LIVAS products, and ESA, who funded the LIVAS project (contract no. 4000104106/11/NL/FF/fk).

Data Availability: The model outputs and the data used for the analysis are available upon request from Vassilis Amiridis (vamoir@noa.gr) and/or Eleni Drakaki (eldrakaki@noa.gr). The LIVAS dust products are available upon request from Vassilis Amiridis (vamoir@noa.gr), Emmanouil Proestakis (proestakis@noa.gr), and/or Eleni Marinou (elmarinou@noa.gr). The MIDAS dataset has been developed in the framework of the DUST-GLASS project (grant no.749461; European Union's Horizon 2020 Research and Innovation programme under the Marie Skłodowska-Curie Actions) and it is available at: https://doi.org/10.5281/zenodo.4244106

Code Availability: The source code of WRF-L is available upon request from Vassilis Amiridis (vamoir@noa.gr) and/or Eleni Drakaki (eldrakaki@noa.gr).

References

Amiridis, V., Wandinger, U., Marinou, E., Giannakaki, E., Tsekeri, A., Basart, S., Kazadzis, S., Gkikas, A., Taylor, M., Baldasano, J. and Ansmann, A.: Optimizing CALIPSO Saharan dust retrievals, Atmos. Chem. Phys., 13(23), 12089–12106, doi:10.5194/acp-13-12089-2013, 2013.

Amiridis, V., Marinou, E., Tsekeri, A., Wandinger, U., Schwarz, A., Giannakaki, E., Mamouri, R., Kokkalis, P., Binietoglou, I., Solomos, S., Herekakis, T., Kazadzis, S., Gerasopoulos, E., Proestakis, E., Kottas, M., Balis, D., Papayannis, A., Kontoes, C., Kourtidis, K., Papagiannopoulos, N., Mona, L., Pappalardo, G., Le Rille, O. and Ansmann, A.: LIVAS: a 3-D multi-wavelength aerosol/cloud database based on CALIPSO and EARLINET, Atmos. Chem. Phys., 15(13), 7127–7153, doi:10.5194/acp-15-7127-2015, 2015.

Basart, S., Vendrell, L. and Baldasano, J. M.: High-resolution dust modelling over complex terrains in West Asia, Aeolian Res., 23, 37–50, doi:10.1016/j.aeolia.2016.09.005, 2016.

Bullard, J. E., Baddock, M., Bradwell, T., Crusius, J., Darlington, E., Gaiero, D., Gassó, S., Gisladottir, G., Hodgkins, R., McCulloch, R., McKenna-Neuman, C., Mockford, T., Stewart, H. and Thorsteinsson, T.: High-latitude dust in the Earth system, Rev. Geophys., 54(2), 447–485, doi:10.1002/2016RG000518, 2016.

Chen, F. and Dudhia, J.: Coupling an advanced land surface-hydrology model with the Penn-State-NCAR MM5 modeling system. Part II: Preliminary model validation, Mon. Weather Rev., 129(4), 587–604, doi:10.1175/1520-0493(2001)129<0587:CAALSH>2.0.CO;2, 2001.

Clift, R. and Gauvin, W. H.: Motion of entrained particles in gas streams, Can. J. Chem. Eng., 49(4), 439–448, doi:10.1002/cjce.5450490403, 1971.

Daskalopoulou, V., Mallios, S. A., Ulanowski, Z., Hloupis, G., Gialitaki, A., Tsikoudi, I., Tassis, K. and Amiridis, V.: The electrical activity of Saharan dust as perceived from surface electric field observations, Atmos. Chem. Phys., 21(2), 927–949, doi:10.5194/acp-21-927-2021, 2021.

Diehl, K., Debertshäuser, M., Eppers, O., Schmithüsen, H., Mitra, S. K. and Borrmann, S.: Particle surface area dependence of mineral dust in immersion freezing mode: Investigations with freely suspended drops in an acoustic levitator and a vertical wind tunnel, Atmos. Chem. Phys., 14(22), 12343–12355, doi:10.5194/acp-14-12343-2014, 2014.

van der Does, M., Knippertz, P., Zschenderlein, P., Giles Harrison, R. and Stuut, J. B. W.: The mysterious long-range transport of giant mineral dust particles, Sci. Adv., 4(12), eaau2768, doi:10.1126/sciadv.aau2768, 2018.

Du, Y., Xu, X., Chu, M., Guo, Y. and Wang, J.: Air particulate matter and cardiovascular disease: The epidemiological, biomedical and clinical evidence, J. Thorac. Dis., 8(1), E8–E19, doi:10.3978/j.issn.2072-1439.2015.11.37, 2016.

Escribano, J., Di Tomaso, E., Jorba, O., Klose, M., Gonçalves Ageitos, M., Macchia, F., Amiridis, V., Baars, H., Marinou, E., Proestakis, E., Urbanneck, C., Althausen, D., Bühl, J., Mamouri, R.-E., and Pérez García-Pando, C.: Assimilating spaceborne lidar dust extinction can improve dust forecasts, Atmos. Chem. Phys., 22, 535–560, https://doi.org/10.5194/acp-22-535-2022, 2022.

Gasteiger, J., Groß, S., Sauer, D., Haarig, M., Ansmann, A. and Weinzierl, B.: Particle settling and vertical mixing in the Saharan Air Layer as seen from an integrated model, lidar, and in situ perspective, Atmos. Chem. Phys., 17(1), 297–311, doi:10.5194/acp-17-297-2017, 2017.

Gelaro, R., McCarty, W., Suárez, M. J., Todling, R., Molod, A., Takacs, L., Randles, C. A., Darmenov, A., Bosilovich, M. G., Reichle, R., Wargan, K., Coy, L., Cullather, R., Draper, C., Akella, S., Buchard, V., Conaty, A., da Silva, A. M., Gu, W., Kim, G., Koster, R., Lucchesi, R., Merkova, D., Nielsen, J. E., Partyka, G., Pawson, S., Putman, W., Rienecker, M., Schubert, S. D., Sienkiewicz, M., & Zhao, B.: The Modern-Era Retrospective Analysis for Research and Applications, Version 2 (MERRA-2), *Journal of Climate*, *30*(14), 5419-5454. Retrieved Feb 4, 2022, from https://journals.ametsoc.org/view/journals/clim/30/14/jcli-d-16-0758.1.xml, 2017

Georgoulias, A. K., Alexandri, G., Kourtidis, K. A., Lelieveld, J., Zanis, P., Pöschl, U., Levy, R., Amiridis, V., Marinou, E., and Tsikerdekis, A.: Spatiotemporal variability and contribution of different aerosol types to the aerosol optical depth over the Eastern Mediterranean, Atmos. Chem. Phys., 16, 13853–13884, https://doi.org/10.5194/acp-16-13853-2016, 2016.

Georgoulias, A. K., Tsikerdekis, A., Amiridis, V., Marinou, E., Benedetti, A., Zanis, P., Alexandri, G., Mona, L., Kourtidis, K. A. and Lelieveld, J.: A 3-D evaluation of the MACC reanalysis dust product over Europe, northern Africa and Middle East

using CALIOP/CALIPSO dust satellite observations, Atmos. Chem. Phys., 18(12), 8601–8620, doi:10.5194/acp-18-8601-2018, 2018.

Georgoulias, A.K.; Marinou, E.; Tsekeri, A.; Proestakis, E.; Akritidis, D.; Alexandri, G.; Zanis, P.; Balis, D.; Marenco, F.; Tesche, M.; Amiridis, V. A First Case Study of CCN Concentrations from Spaceborne Lidar Observations. *Remote Sens.*, *12*, 1557. https://doi.org/10.3390/rs12101557, 2020

Giannadaki, D., Pozzer, A. and Lelieveld, J.: Modeled global effects of airborne desert dust on air quality and premature mortality, Atmos. Chem. Phys., 14(2), 957–968, doi:10.5194/acp-14-957-2014, 2014.

Ginoux, P.: Effects of nonsphericity on mineral dust modeling, J. Geophys. Res. Atmos., 108(2), doi:10.1029/2002jd002516, 2003a.

Ginoux, P.: Effects of nonsphericity on mineral dust modeling, J. Geophys. Res., 108(D2), doi:10.1029/2002jd002516, 2003b.

Ginoux, P., Chin, M., Tegen, I., Goddard, T. and In-, G.: Sources and distributions of dust aerosols simulated with the GOCART model, J. Geophys. Res., 106, 20255–20273, 2001.

Ginoux, P., Prospero, J. M., Gill, T. E., Hsu, N. C. and Zhao, M.: Global-scale attribution of anthropogenic and natural dust sources and their emission rates based on MODIS Deep Blue aerosol products, Rev. Geophys., 50(3), 1–36, doi:10.1029/2012RG000388, 2012.

Gkikas, A., Proestakis, E., Amiridis, V., Kazadzis, S., Di Tomaso, E., Tsekeri, A., Marinou, E., Hatzianastassiou, N. and Pérez Garciá-Pando, C.: ModIs Dust AeroSol (MIDAS): A global fine-resolution dust optical depth data set, Atmos. Meas. Tech., 14(1), 309–334, doi:10.5194/amt-14-309-2021, 2021.

Goudie, A. S.: Desert dust and human health disorders, Environ. Int., 63, 101–113, doi:10.1016/j.envint.2013.10.011, 2014.

Goudie, A. S. and Middleton, N. J.: Desert Dust in the Global System., 2006.

Grell, G. A. and Dévényi, D.: A generalized approach to parameterizing convection combining ensemble and data assimilation techniques, Geophys. Res. Lett., 29(14), 10–13, doi:10.1029/2002GL015311, 2002.

Gu, Z., He, Y., Zhang, Y., Su, J., Zhang, R., Yu, C. W. and Zhang, D.: An overview of triggering mechanisms and characteristics of local strong sandstorms in china and haboobs, Atmosphere (Basel)., 12(6), 1–17, doi:10.3390/atmos12060752, 2021.

Harb, K., Butt, O., Abdul-jauwad, S. and Al-yami, A. M.: Systems Adaptation for Satellite Signal under Dust , Sand and Gaseous Attenuations, J. Wirel. Netw. Commun., 3(3), 39–49, doi:10.5923/j.jwnc.20130303.03, 2013.

Huang, Y., Kok, J. F., Kandler, K., Lindqvist, H., Nousiainen, T., Sakai, T., Adebiyi, A. and Jokinen, O.: Climate Models and Remote Sensing Retrievals Neglect Substantial Desert Dust Asphericity, Geophys. Res. Lett., 47(6), 1–11, doi:10.1029/2019GL086592, 2020.

Huneeus, N., Schulz, M., Balkanski, Y., Griesfeller, J., Prospero, J., Kinne, S., Bauer, S., Boucher, O., Chin, M., Dentener, F., Diehl, T., Easter, R., Fillmore, D., Ghan, S., Ginoux, P., Grini, A., Horowitz, L., Koch, D., Krol, M. C., Landing, W., Liu, X., Mahowald, N., Miller, R., Morcrette, J. J., Myhre, G., Penner, J., Perlwitz, J., Stier, P., Takemura, T. and Zender, C. S.: Global

dust model intercomparison in AeroCom phase i, Atmos. Chem. Phys., 11(15), 7781–7816, doi:10.5194/acp-11-7781-2011, 2011.

Iacono, M. J., Delamere, J. S., Mlawer, E. J., Shephard, M. W., Clough, S. A. and Collins, W. D.: Radiative forcing by long-lived greenhouse gases: Calculations with the AER radiative transfer models, J. Geophys. Res. Atmos., 113(13), 2–9, doi:10.1029/2008JD009944, 2008.

Jennings, S. G.: The mean free path in air, J. Aerosol Sci., 19(2), 159–166, doi:10.1016/0021-8502(88)90219-4, 1988.

Jickells, T., Boyd, P. and Hunter, K. A.: Biogeochemical Impacts of Dust on the Global Carbon Cycle, in Mineral Dust: A Key Player in the Earth System, edited by P. Knippertz and J.-B. W. Stuut, pp. 359–384, Springer Netherlands, Dordrecht., 2014.

Jickells, T. D., An, Z. S., Andersen, K. K., Baker, A. R., Bergametti, C., Brooks, N., Cao, J. J., Boyd, P. W., Duce, R. A., Hunter, K. A., Kawahata, H., Kubilay, N., LaRoche, J., Liss, P. S., Mahowald, N., Prospero, J. M., Ridgwell, A. J., Tegen, I. and Torres, R.: Global iron connections between desert dust, ocean biogeochemistry, and climate, Science (80-.)., 308(5718), 67–71, doi:10.1126/science.1105959, 2005.

Jiménez, P. A. and Dudhia, J.: Improving the representation of resolved and unresolved topographic effects on surface wind in the wrf model, J. Appl. Meteorol. Climatol., 51(2), 300–316, doi:10.1175/JAMC-D-11-084.1, 2012.

Knippertz, P. and Stuut, J. B. W.: Mineral dust: A key player in the earth system, Miner. Dust A Key Play. Earth Syst., 1–509, doi:10.1007/978-94-017-8978-3, 2014.

Kok, J. F.: An improved parameterization of wind-blown sand flux on Mars that includes the effect of hysteresis, Geophys. Res. Lett., 37(12), doi:10.1029/2010GL043646, 2010.

Kok, J. F.: A scaling theory for the size distribution of emitted dust aerosols suggests climate models underestimate the size of the global dust cycle, Proc. Natl. Acad. Sci. U. S. A., 108(3), 1016–1021, doi:10.1073/pnas.1014798108, 2011.

Kok, J. F., Adebiyi, A. A., Albani, S., Balkanski, Y., Checa-Garcia, R., Chin, M., Colarco, P. R., Hamilton, D. S., Huang, Y., Ito, A., Klose, M., Li, L., Mahowald, N. M., Miller, R. L., Obiso, V., Pérez García-Pando, C., Rocha-Lima, A. and Wan, J. S.: Contribution of the world's main dust source regions to the global cycle of desert dust, Atmos. Chem. Phys., 21(10), 8169–8193, doi:10.5194/acp-21-8169-2021, 2021.

Konsta, D., Binietoglou, I., Gkikas, A., Solomos, S., Marinou, E., Proestakis, E., Basart, S., García-Pando, C. P., El-Askary, H. and Amiridis, V.: Evaluation of the BSC-DREAM8b regional dust model using the 3D LIVAS-CALIPSO product, Atmos. Environ., 195, 46–62, doi:10.1016/j.atmosenv.2018.09.047, 2018.

Kosmopoulos, P. G., Kazadzis, S., El-Askary, H., Taylor, M., Gkikas, A., Proestakis, E., Kontoes, C. and El-Khayat, M. M.: Earth-observation-based estimation and forecasting of particulate matter impact on solar energy in Egypt, Remote Sens., 10(12), 1–23, doi:10.3390/rs10121870, 2018.

LeGrand, S. L., Polashenski, C., Letcher, T. W., Creighton, G. A., Peckham, S. E. and Cetola, J. D.: The AFWA dust emission scheme for the GOCART aerosol model in WRF-Chem v3.8.1, Geosci. Model Dev., 12(1), 131–166, doi:10.5194/gmd-12-131-2019, 2019.

Li, J. and Osada, K.: Preferential settling of elongated mineral dust particles in the atmosphere, Geophys. Res. Lett., 34(17), 2–5, doi:10.1029/2007GL030262, 2007.

Liu, D., Taylor, J. W., Crosier, J., Marsden, N., Bower, K. N., Lloyd, G., Ryder, C. L., Brooke, J. K., Cotton, R., Marenco, F., Blyth, A., Cui, Z., Estelles, V., Gallagher, M., Coe, H. and Choularton, T. W.: Aircraft and ground measurements of dust aerosols over the west African coast in summer 2015 during ICE-D and AER-D, Atmos. Chem. Phys., 18(5), 3817–3838, doi:10.5194/acp-18-3817-2018, 2018.

Loth, E.: Drag of non-spherical solid particles of regular and irregular shape, Powder Technol., 182(3), 342–353, doi:10.1016/j.powtec.2007.06.001, 2008.

Mahowald, N., Albani, S., Kok, J. F., Engelstaeder, S., Scanza, R., Ward, D. S. and Flanner, M. G.: The size distribution of desert dust aerosols and its impact on the Earth system, Aeolian Res., 15, 53–71, doi:10.1016/j.aeolia.2013.09.002, 2014.

Mallios, S. A., Drakaki, E. and Amiridis, V.: Effects of dust particle sphericity and orientation on their gravitational settling in the earth's atmosphere, J. Aerosol Sci., 150(April), 105634, doi:10.1016/j.jaerosci.2020.105634, 2020.

Mallios, S. A., Papangelis, G., Hloupis, G., Papaioannou, A., Daskalopoulou, V. and Amiridis, V.: Modeling of Spherical Dust Particle Charging due to Ion Attachment, Front. Earth Sci., 9(August), 1–22, doi:10.3389/feart.2021.709890, 2021.

Maring, H., Savoie, D. L., Izaguirre, M. A., Custals, L. and Reid, J. S.: Mineral dust aerosol size distribution change during atmospheric transport, J. Geophys. Res. Atmos., 108(19), 1–6, doi:10.1029/2002jd002536, 2003.

Marinou, E., Amiridis, V., Binietoglou, I., Tsikerdekis, A., Solomos, S., Proestakis, E., Konsta, Di., Papagiannopoulos, N., Tsekeri, A., Vlastou, G., Zanis, P., Balis, Di., Wandinger, U. and Ansmann, A.: Three-dimensional evolution of Saharan dust transport towards Europe based on a 9-year EARLINET-optimized CALIPSO dataset, Atmos. Chem. Phys., 17(9), 5893–5919, doi:10.5194/acp-17-5893-2017, 2017.

Marinou, E., Tesche, M., Nenes, A., Ansmann, A., Schrod, J., Mamali, D., Tsekeri, A., Pikridas, M., Baars, H., Engelmann, R., Voudouri, K. A., Solomos, S., Sciare, J., Groß, S., Ewald, F. and Amiridis, V.: Retrieval of ice-nucleating particle concentrations from lidar observations and comparison with UAV in situ measurements, Atmos. Chem. Phys., 19(17), 11315–11342, doi:10.5194/acp-19-11315-2019, 2019.

Morrison, H., Curry, J. A. and Khvorostyanov, V. I.: A new double-moment microphysics parameterization for application in cloud and climate models. Part I: Description, J. Atmos. Sci., 62(6), 1665–1677, doi:10.1175/JAS3446.1, 2005.

Nakanishi, M. and Niino, H.: An improved Mellor-Yamada Level-3 model: Its numerical stability and application to a regional prediction of advection fog, Boundary-Layer Meteorol., 119(2), 397–407, doi:10.1007/s10546-005-9030-8, 2006.

Nicoll, K. A., Harrison, R. G. and Ulanowski, Z.: Observations of Saharan dust layer electrification, Environ. Res. Lett., 6(1), 1–8, doi:10.1088/1748-9326/6/1/014001, 2011.

O'Sullivan, D., Marenco, F., Ryder, C., Pradhan, Y., Kipling, Z., Johnson, B., Benedetti, A., Brooks, M., McGill, M., Yorks, J. and Selmer, P.: Models transport Saharan dust too low in the atmosphere compared to observations, Atmos. Chem. Phys. Discuss., 1–47, doi:10.5194/acp-2020-57, 2020.

Okin, G. S., Mahowald, N., Chadwick, O. A. and Artaxo, P.: Impact of desert dust on the biogeochemistry of phosphorus in terrestrial ecosystems, Global Biogeochem. Cycles, 18(2), doi:10.1029/2003GB002145, 2004.

Petters, M. D. and Kreidenweis, S. M.: A single parameter representation of hygroscopic growth and cloud condensation nucleus activity-Part 3: Including surfactant partitioning, Atmos. Chem. Phys., 13(2), 1081–1091, doi:10.5194/acp-13-1081-2013, 2013.

Proestakis, E., Amiridis, V., Marinou, E., Georgoulias, A. K., Solomos, S., Kazadzis, S., Chimot, J., Che, H., Alexandri, G., Binietoglou, I., Daskalopoulou, V., Kourtidis, K. A., De Leeuw, G. and Van Der A, R. J.: Nine-year spatial and temporal evolution of desert dust aerosols over South and East Asia as revealed by CALIOP, Atmos. Chem. Phys., 18(2), 1337–1362, doi:10.5194/acp-18-1337-2018, 2018.

Prospero, J. M., Bonatti, E., Schubert, C. and Carlson, T. N.: Dust in the Caribbean atmosphere traced to an African dust storm, Earth Planet. Sci. Lett., 9(3), 287–293, doi:10.1016/0012-821X(70)90039-7, 1970.

Prospero, J. M., Ginoux, P., Torres, O., Nicholson, S. E. and Gill, T. E.: Environmental characterization of global sources of atmospheric soil dust identified with the Nimbus 7 Total Ozone Mapping Spectrometer (TOMS) absorbing aerosol product, Rev. Geophys., 40(1), 2-1-2–31, doi:10.1029/2000RG000095, 2002.

Renard, J. B., Dulac, F., Durand, P., Bourgeois, Q., Denjean, C., Vignelles, D., Couté, B., Jeannot, M., Verdier, N. and Mallet, M.: In situ measurements of desert dust particles above the western Mediterranean Sea with the balloon-borne Light Optical Aerosol Counter/sizer (LOAC) during the ChArMEx campaign of summer 2013, Atmos. Chem. Phys., 18(5), 3677–3699, doi:10.5194/acp-18-3677-2018, 2018.

Ryder, C. L., Highwood, E. J., Lai, T. M., Sodemann, H. and Marsham, J. H.: Impact of atmospheric transport on the evolution of microphysical and optical properties of Saharan dust, Geophys. Res. Lett., 40(10), 2433–2438, doi:10.1002/grl.50482, 2013a.

Ryder, C. L., Highwood, E. J., Rosenberg, P. D., Trembath, J., Brooke, J. K., Bart, M., Dean, A., Crosier, J., Dorsey, J., Brindley, H., Banks, J., Marsham, J. H., McQuaid, J. B., Sodemann, H. and Washington, R.: Optical properties of Saharan dust aerosol and contribution from the coarse mode as measured during the Fennec 2011 aircraft campaign, Atmos. Chem. Phys., 13(1), 303–325, doi:10.5194/acp-13-303-2013, 2013b.

Ryder, C. L., Marenco, F., Brooke, J. K., Estelles, V., Cotton, R., Formenti, P., McQuaid, J. B., Price, H. C., Liu, D., Ausset, P., Rosenberg, P. D., Taylor, J. W., Choularton, T., Bower, K., Coe, H., Gallagher, M., Crosier, J., Lloyd, G., Highwood, E. J. and Murray, B. J.: Coarse-mode mineral dust size distributions, composition and optical properties from AER-D aircraft measurements over the tropical eastern Atlantic, Atmos. Chem. Phys., 18(23), 17225–17257, doi:10.5194/acp-18-17225-2018, 2018a.

Ryder, C. L., Highwood, E. J., Walser, A., Seibert, P., Philipp, A. and Weinzierl, B.: Coarse and giant particles are ubiquitous in Saharan dust export regions and are radiatively significant over the Sahara, Atmos. Chem. Phys., 19(24), 15353–15376, doi:10.5194/acp-19-15353-2019, 2019.

Sanjeevi, S. K. P., Kuipers, J. A. M. and Padding, J. T.: Drag, lift and torque correlations for non-spherical particles from Stokes limit to high Reynolds numbers, Int. J. Multiph. Flow, 106, 325–337, doi:10.1016/j.ijmultiphaseflow.2018.05.011, 2018.

Shao, B., Liu, G. R., Lin, T., Xu, G. X. and Yan, X.: Rotation and orientation of irregular particles in viscous fluids using the gradient smoothed method (GSM), Eng. Appl. Comput. Fluid Mech., 11(1), 557–575, doi:10.1080/19942060.2017.1329169, 2017.

Solomos, S., Kallos, G., Kushta, J., Astitha, M., Tremback, C., Nenes, A. and Levin, Z.: An integrated modeling study on the effects of mineral dust and sea salt particles on clouds and precipitation, Atmos. Chem. Phys., 11(2), 873–892, doi:10.5194/acp-11-873-2011, 2011.

Solomos, S., Kallos, G., Mavromatidis, E. and Kushta, J.: Density currents as a desert dust mobilization mechanism, Atmos. Chem. Phys., 12(22), 11199–11211, doi:10.5194/acp-12-11199-2012, 2012.

Solomos, S., Ansmann, A., Mamouri, R.-E., Binietoglou, I., Patlakas, P., Marinou, E., and Amiridis, V.: Remote sensing and modelling analysis of the extreme dust storm hitting the Middle East and eastern Mediterranean in September 2015, Atmos. Chem. Phys., 17, 4063–4079, https://doi.org/10.5194/acp-17-4063-2017, 2017.

Stockdale, A., Krom, M. D., Mortimer, R. J. G., Benning, L. G., Carslaw, K. S., Herbert, R. J., Shi, Z., Myriokefalitakis, S., Kanakidou, M. and Nenes, A.: Understanding the nature of atmospheric acid processing of mineral dusts in supplying bioavailable phosphorus to the oceans, Proc. Natl. Acad. Sci. U. S. A., 113(51), 14639–14644, doi:10.1073/pnas.1608136113, 2016.

Tagliabue, A., Bowie, A. R., Boyd, P. W., Buck, K. N., Johnson, K. S. and Saito, M. A.: The integral role of iron in ocean biogeochemistry, Nature, 543(7643), 51–59, doi:10.1038/nature21058, 2017.

Tesche, M., Ansmann, A., Müller, D., Althausen, D., Mattis, I., Heese, B., Freudenthaler, V., Wiegner, M., Esselborn, M., Pisani, G. and Knippertz, P.: Vertical profiling of Saharan dust with Raman lidars and airborne HSRL in southern Morocco during SAMUM, Tellus, Ser. B Chem. Phys. Meteorol., 61(1), 144–164, doi:10.1111/j.1600-0889.2008.00390.x, 2009.

Textor, C., Schulz, M., Guibert, S., Kinne, S., Balkanski, Y., Bauer, S., Berntsen, T., Berglen, T., Boucher, O., Chin, M., Dentener, F., Diehl, T., Easter, R., Feichter, H., Fillmore, D., Ghan, S., Ginoux, P., Gong, S., Grini, A., Hendricks, J., Horowitz, L., Huang, P., Isaksen, I., Iversen, T., Kloster, S., Koch, D., Kirkevåg, A., Kristjansson, J. E., Krol, M., Lauer, A., Lamarque, J. F., Liu, X., Montanaro, V., Myhre, G., Penner, J., Pitari, G., Reddy, S., Seland, Stier, P., Takemura, T. and Tie, X.: Analysis and quantification of the diversities of aerosol life cycles within AeroCom, Atmos. Chem. Phys., 6(7), 1777–1813, doi:10.5194/acp-6-1777-2006, 2006.

Toth III, J., Rajupet, S., Squire, H., Volbers, B., Zhou, J., Xie, L., Sankaran, R. M. and Lacks, D.: Electrostatic forces alter particle size distributions in atmospheric dust, Atmos. Chem. Phys. Discuss., 1–14, doi:10.5194/acp-2019-650, 2019.

Tsikerdekis, A., Zanis, P., Steiner, A. L., Solmon, F., Amiridis, V., Marinou, E., Katragkou, E., Karacostas, T., and Foret, G.: Impact of dust size parameterizations on aerosol burden and radiative forcing in RegCM4, Atmos. Chem. Phys., 17, 769–791, https://doi.org/10.5194/acp-17-769-2017, 2017.

Twohy, C. H., Kreidenweis, S. M., Eidhammer, T., Browell, E. V., Heymsfield, A. J., Bansemer, A. R., Anderson, B. E., Chen, G., Ismail, S., DeMott, P. J. and Van Den Heever, S. C.: Saharan dust particles nucleate droplets in eastern Atlantic clouds, Geophys. Res. Lett., 36(1), 1–6, doi:10.1029/2008GL035846, 2009.

Ulanowski, Z., Bailey, J., Lucas, P. W., Hough, J. H. and Hirst, E.: Alignment of atmospheric mineral dust due to electric field, Atmos. Chem. Phys., 7(24), 6161–6173, doi:10.5194/acp-7-6161-2007, 2007.

Weinzierl, B., Petzold, A., Esselborn, M., Wirth, M., Rasp, K., Kandler, K., Schütz, L., Koepke, P. and Fiebig, M.: Airborne measurements of dust layer properties, particle size distribution and mixing state of Saharan dust during SAMUM 2006, Tellus, Ser. B Chem. Phys. Meteorol., 61(1), 96–117, doi:10.1111/j.1600-0889.2008.00392.x, 2009.

Weinzierl, B., Sauer, D., Esselborn, M., Petzold, A., Veira, A., Rose, M., Mund, S., Wirth, M., Ansmann, A., Tesche, M., Gross, S. and Freudenthaler, V.: Microphysical and optical properties of dust and tropical biomass burning aerosol layers in the Cape Verde region-an overview of the airborne in situ and lidar measurements during SAMUM-2, Tellus, Ser. B Chem. Phys. Meteorol., 63(4), 589–618, doi:10.1111/j.1600-0889.2011.00566.x, 2011.

Weinzierl, B., Sauer, D., Minikin, A., Reitebuch, O., Dahlkötter, F., Mayer, B., Emde, C., Tegen, I., Gasteiger, J., Petzold, A., Veira, A., Kueppers, U. and Schumann, U.: On the visibility of airborne volcanic ash and mineral dust from the pilot's perspective in flight, Phys. Chem. Earth, 45–46, 87–102, doi:10.1016/j.pce.2012.04.003, 2012.

Weinzierl, B., Ansmann, A., Prospero, J. M., Althausen, D., Benker, N., Chouza, F., Dollner, M., Farrell, D., Fomba, W. K., Freudenthaler, V., Gasteiger, J., Groß, S., Haarig, M., Heinold, B., Kandler, K., Kristensen, T. B., Mayol-Bracero, O. L., Müller, T., Reitebuch, O., Sauer, D., Schäfler, A., Schepanski, K., Spanu, A., Tegen, I., Toledano, C. and Walser, A.: The Saharan aerosol long-range transport and aerosol-cloud-interaction experiment: Overview and selected highlights, Bull. Am. Meteorol. Soc., 98(7), 1427–1451, doi:10.1175/BAMS-D-15-00142.1, 2017a.

Weinzierl, B., Ansmann, A., Prospero, J. M., Althausen, D., Benker, N., Chouza, F., Dollner, M., Farrell, D., Fomba, W. K., Freudenthaler, V., Gasteiger, J., Groß, S., Haarig, M., Heinold, B., Kandler, K., Kristensen, T. B., Mayol-Bracero, O. L., Müller, T., Reitebuch, O., Sauer, D., Schäfler, A., Schepanski, K., Spanu, A., Tegen, I., Toledano, C. and Walser, A.: The Saharan aerosol long-range transport and aerosol-cloud-interaction experiment: Overview and selected highlights, Bull. Am. Meteorol. Soc., 98(7), 1427–1451, doi:10.1175/BAMS-D-15-00142.1, 2017b.

Winker, D. M., Vaughan, M. A., Omar, A., Hu, Y., Powell, K. A., Liu, Z., Hunt, W. H. and Young, S. A.: Overview of the CALIPSO Mission and CALIOP Data Processing Algorithms, J. Atmos. Ocean. Technol., 26(11), 2310–2323, doi:10.1175/2009JTECHA1281.1, 2009.

Zastawny, M., Mallouppas, G., Zhao, F. and van Wachem, B.: Derivation of drag and lift force and torque coefficients for non-spherical particles in flows, Int. J. Multiph. Flow, 39, 227–239, doi:10.1016/j.ijmultiphaseflow.2011.09.004, 2012.

https://doi.org/10.5194/acp-2022-94
Preprint. Discussion started: 7 April 2022
© Author(s) 2022. CC BY 4.0 License.

Atmospheric Chemistry and Physics Discussions

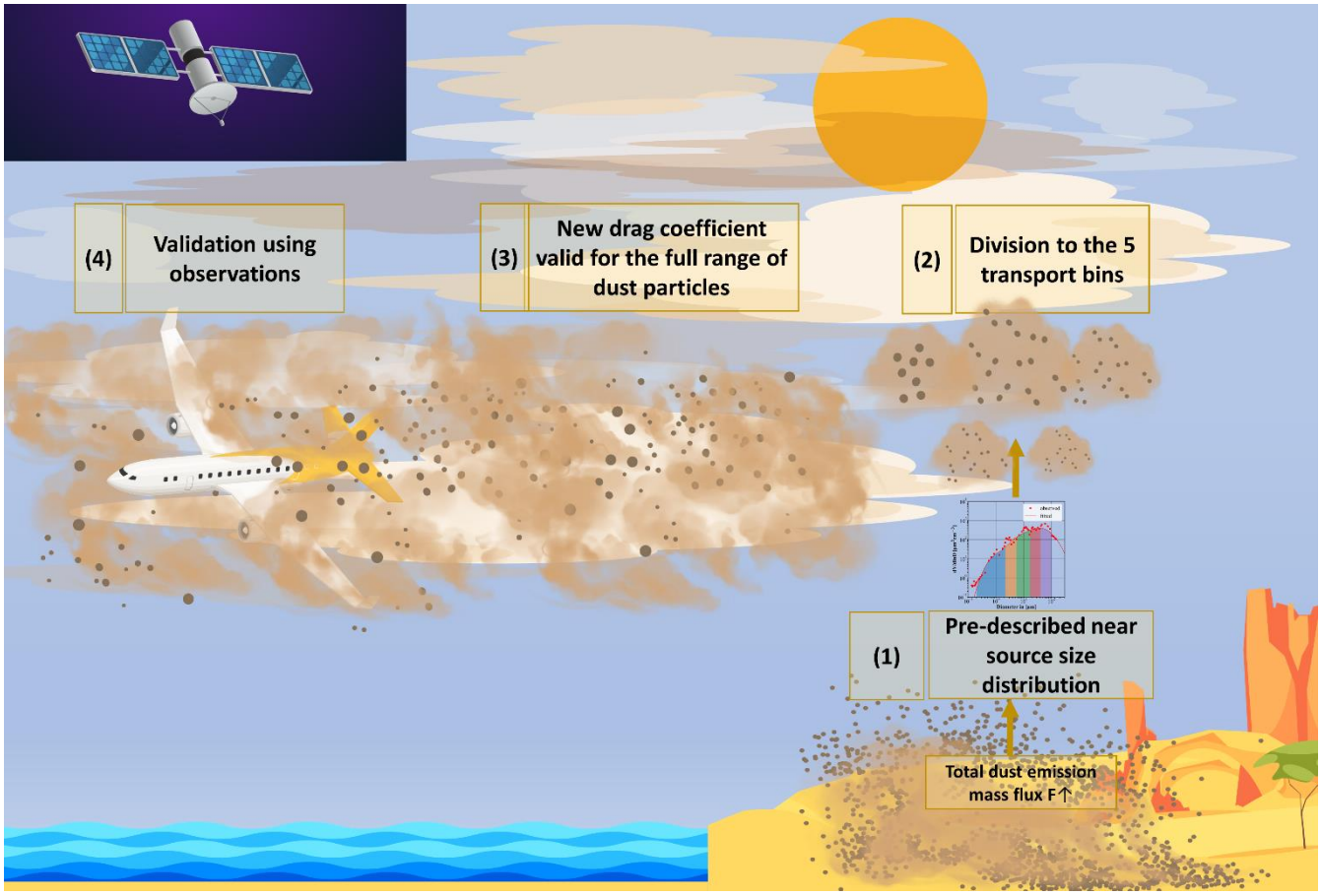

Figure 1: The structure of the presented work. Steps (1), (2) and (3) correspond to the appropriate modifications implemented in the WRF-Chem GOCART-AFWA dust scheme, for the inclusion of the giant dust particles and the development of WRF-L. Step (4) refers to model validation activities.

https://doi.org/10.5194/acp-2022-94
Preprint. Discussion started: 7 April 2022
© Author(s) 2022. CC BY 4.0 License.

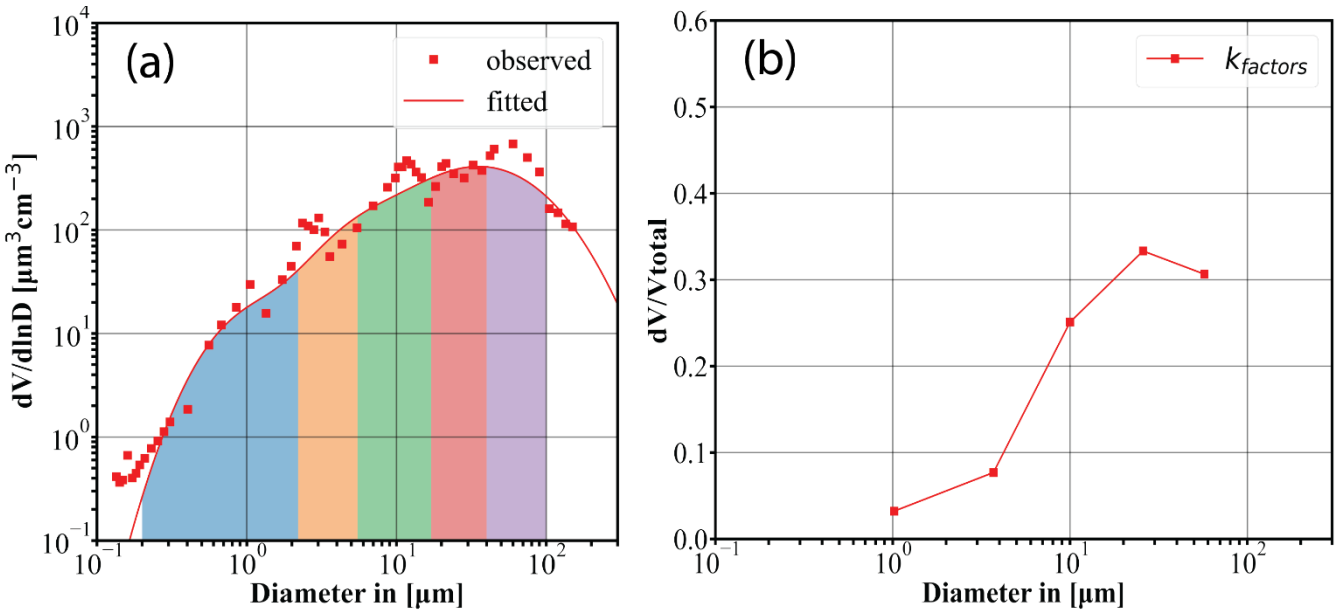

Figure 2: Prescribed dust size distribution used in the WRF-L for the distribution of total dust mass to the transport model size bins: (a) observed FENNEC-PSD (μm^{3}cm^{-3}) (red squares), and the respective fitted volume PSD (black solid line. The shaded areas indicate the model transport size bins in WRF-L. (b) The $k_{factors}$ of the transport size bins, providing the mass fraction of the emitted dust for each bin.

https://doi.org/10.5194/acp-2022-94
Preprint. Discussion started: 7 April 2022
© Author(s) 2022. CC BY 4.0 License.

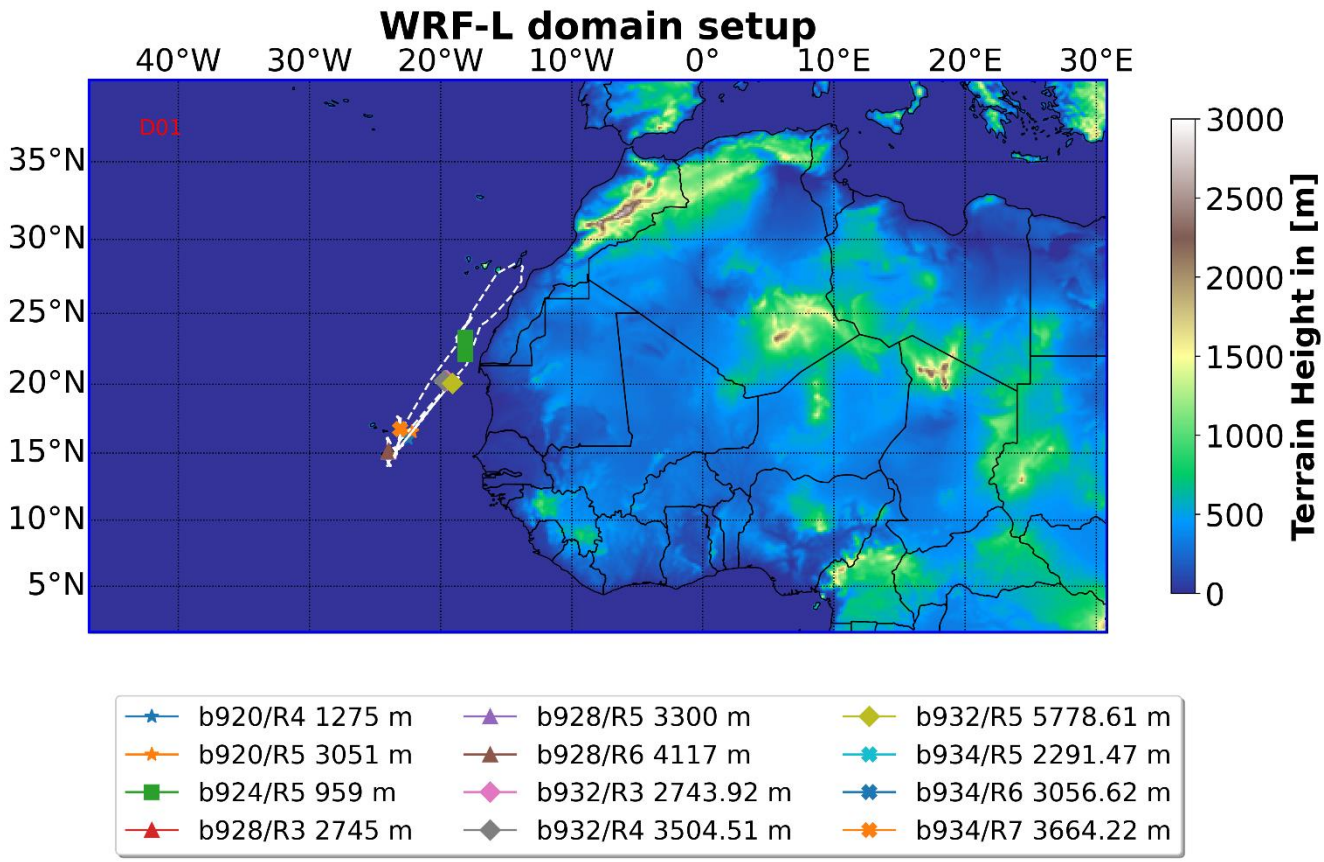

Figure 3: Domain map of the WRF-L model simulations, with horizontal grid spacing of 15km, and 70 vertical levels. The locations of the different runs for the AER-D flights b920, b924, b928, b932 and b932 are also depicted, along with the heights above the sea level (colored markers).

https://doi.org/10.5194/acp-2022-94
Preprint. Discussion started: 7 April 2022
© Author(s) 2022. CC BY 4.0 License.

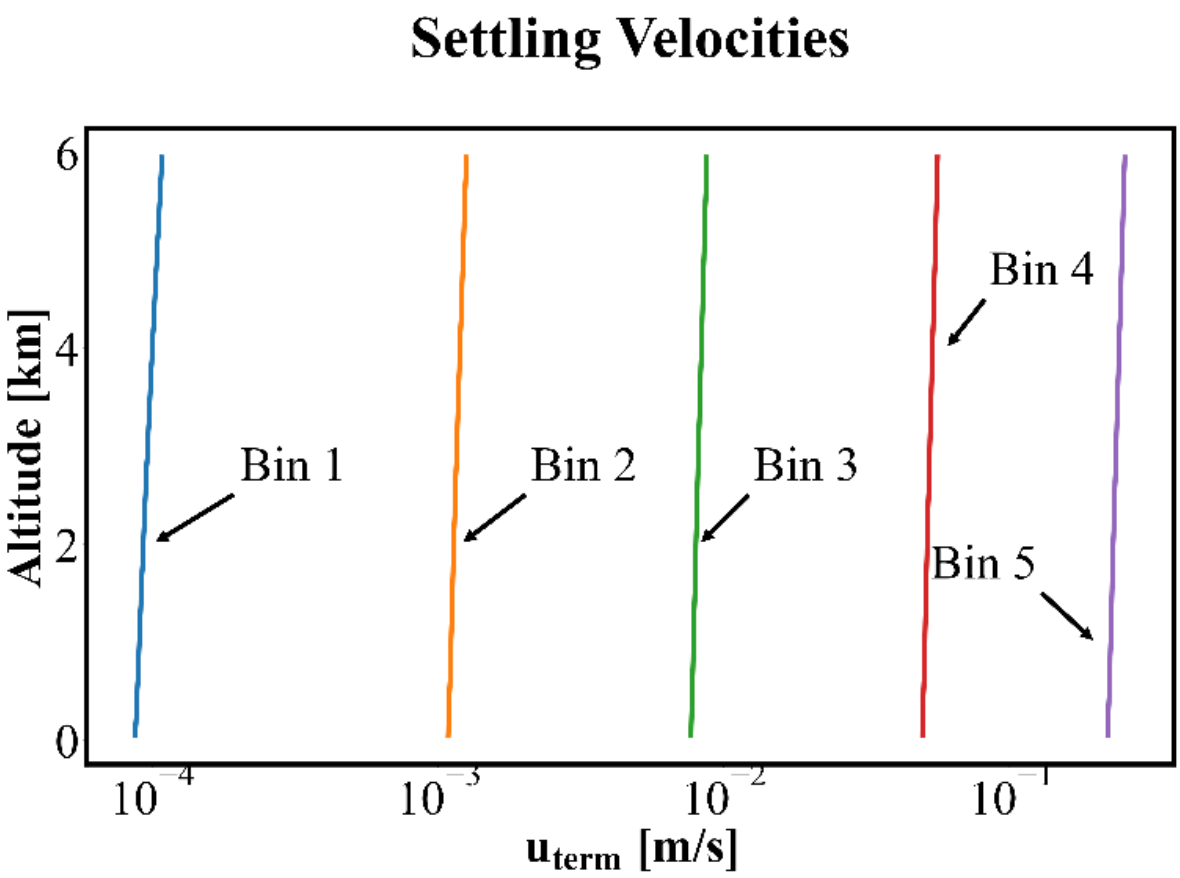

Figure 4: Terminal velocities of the CONTROL experiment, averaged for the simulation time and the domain. Each colored line corresponds to one of the new model size bins, with blue: Bin 1, orange: Bin 2, green: Bin 3, red: Bin 4 and purple: Bin 5.

https://doi.org/10.5194/acp-2022-94
Preprint. Discussion started: 7 April 2022
© Author(s) 2022. CC BY 4.0 License.

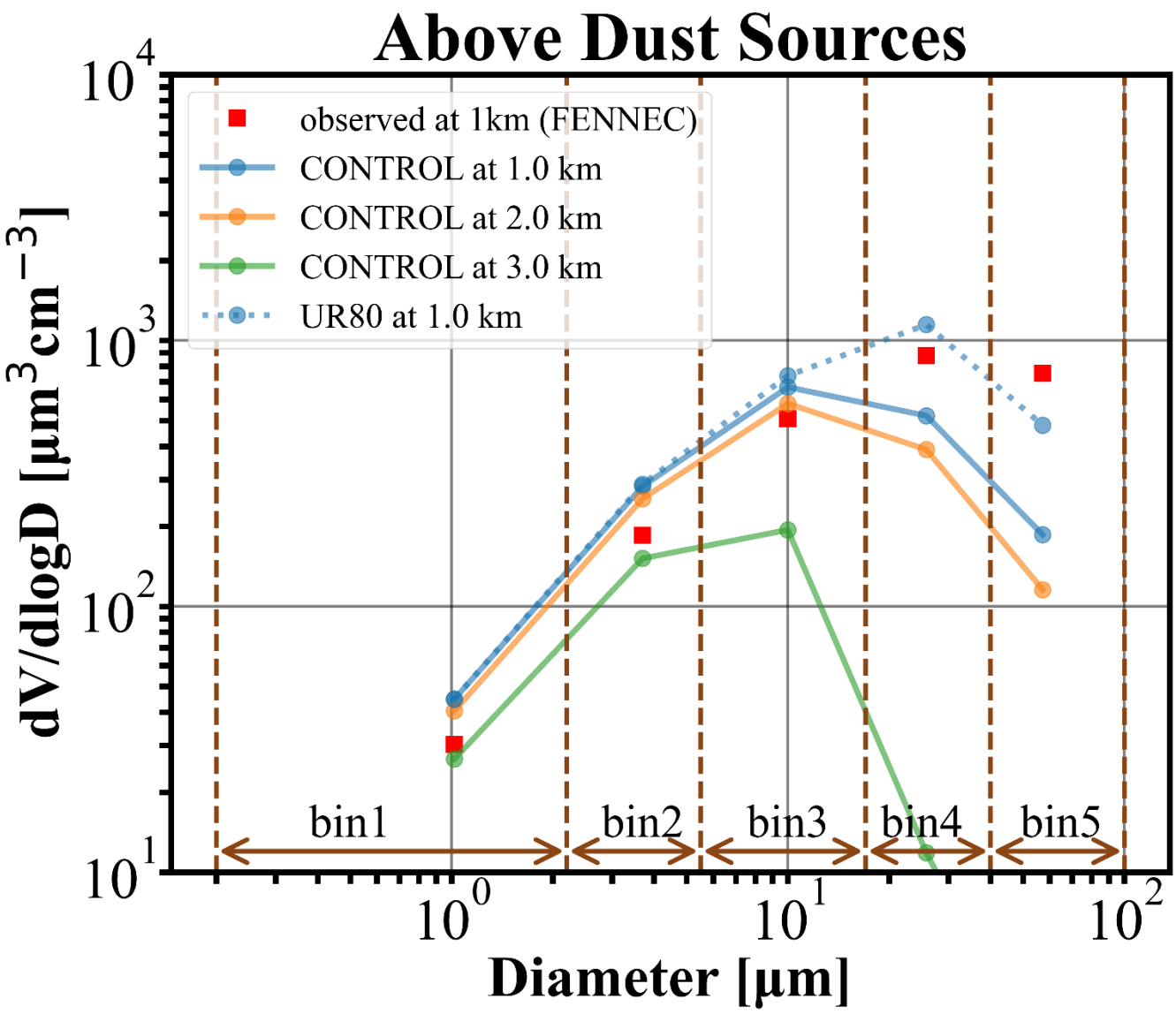

Figure 5: Dust size distribution above an emission point. Blue line: the dust PSD of the CONTROL run at 1 km altitude above the dust source, orange line: the dust PSD of the CONTROL run at 2 km altitude above dust source, green line: the dust PSD of the CONTROL run at 3 km altitude above dust source, blue dotted line: the dust PSD of the UR80 run at 1 km altitude above the dust source and red squares: the mean observed FENNEC-PSD at 1 km altitude.

https://doi.org/10.5194/acp-2022-94
Preprint. Discussion started: 7 April 2022
© Author(s) 2022. CC BY 4.0 License.

Atmospheric Chemistry and Physics Discussions

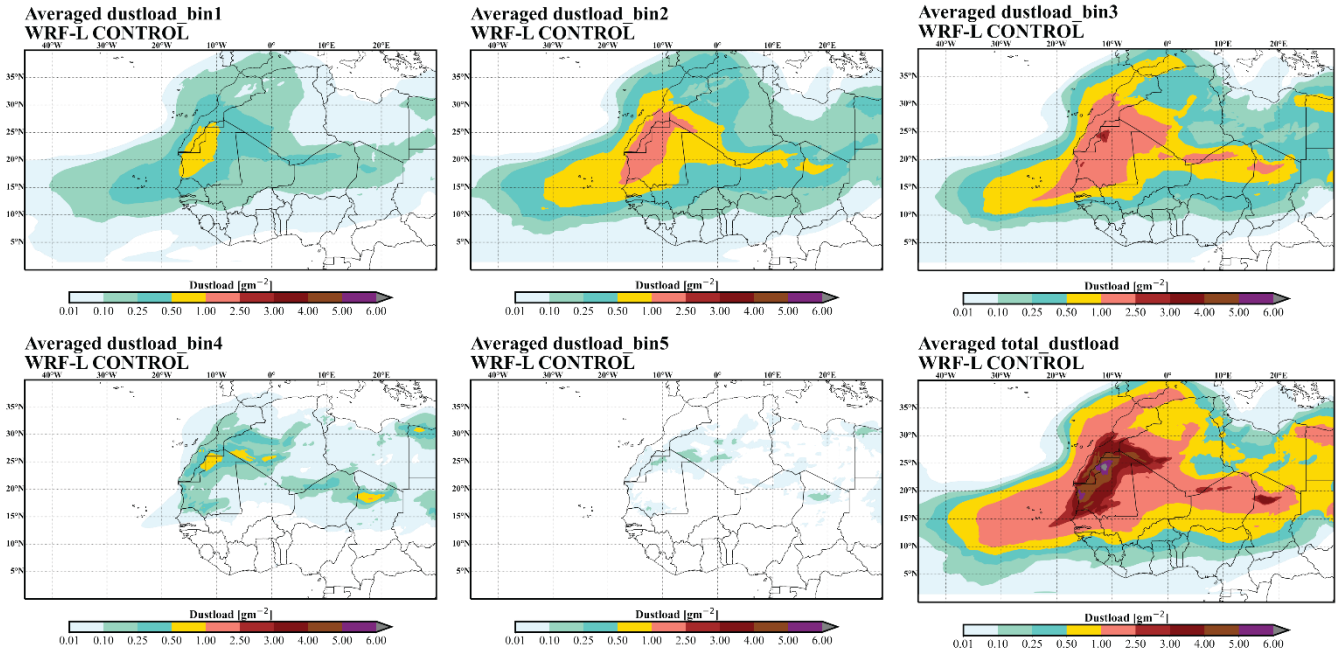

Figure 6: The dust load provided by the model, averaged for the whole simulation period, for (a) bin 1, (b) bin 2, (c) bin 3, (d) bin 4, (e) bin 5, and (f) the whole range of the PSD. The dust load is in g/m^2.

https://doi.org/10.5194/acp-2022-94
Preprint. Discussion started: 7 April 2022
© Author(s) 2022. CC BY 4.0 License.

Atmospheric Chemistry and Physics Discussions

(a)

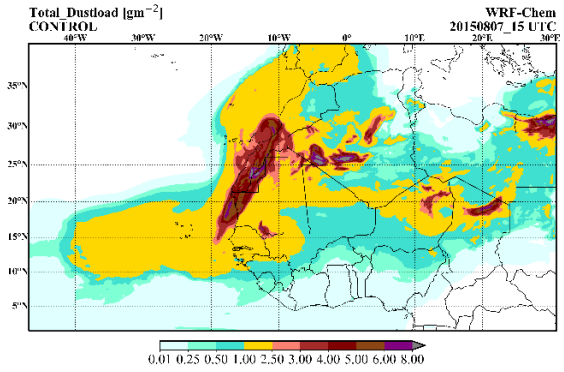

(b)

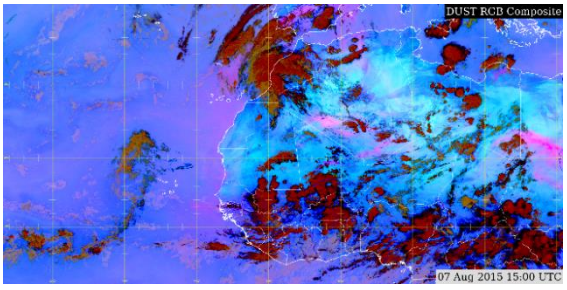

(c)

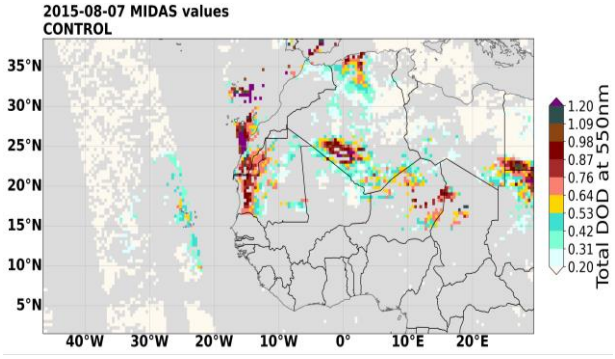

(d)

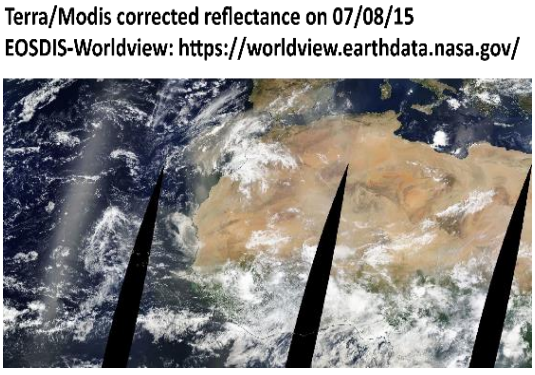

(e)

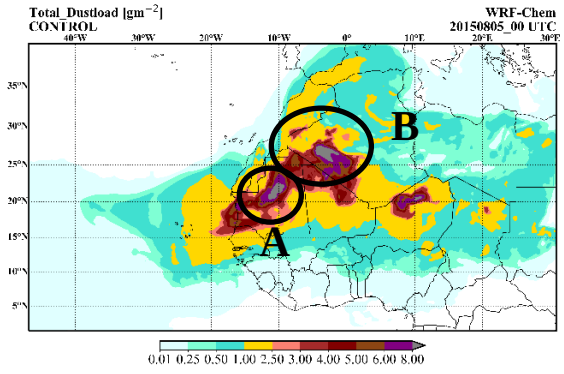

(f)

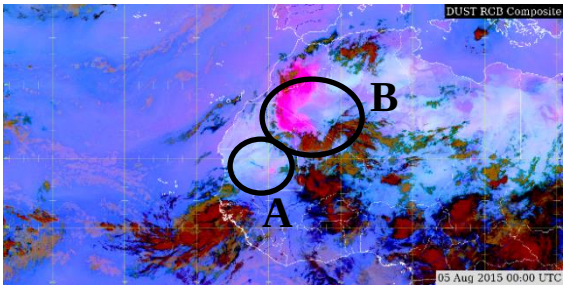

https://doi.org/10.5194/acp-2022-94
Preprint. Discussion started: 7 April 2022
© Author(s) 2022. CC BY 4.0 License.

Figure 7: (a) Modelled dust load and (b) Dust RGB-Colors image from the MSG-SEVIRI. The fuchsia/pink colors indicate dust particles, with darker hue corresponding to higher concentrations or/and dust at higher altitudes. Both (a) and (b) show simulations and measurements, respectively, on 07/08/2015, at 15 UTC, near the time of b920 AER-D flight, at 15:24 -17:00 UTC. (c) MIDAS DOD at 550 µm, on 07/08/2015, and (d) corrected reflectance of Terra/MODIS on 07/08/2015. (e) Modelled dust load on 05/08/2015, at 00 UTC, and (f) Dust RGB image from the MSG-SEVIRI, on 05/08/2015, at 00 UTC.

https://doi.org/10.5194/acp-2022-94
Preprint. Discussion started: 7 April 2022
© Author(s) 2022. CC BY 4.0 License.

Atmospheric Chemistry and Physics Discussions

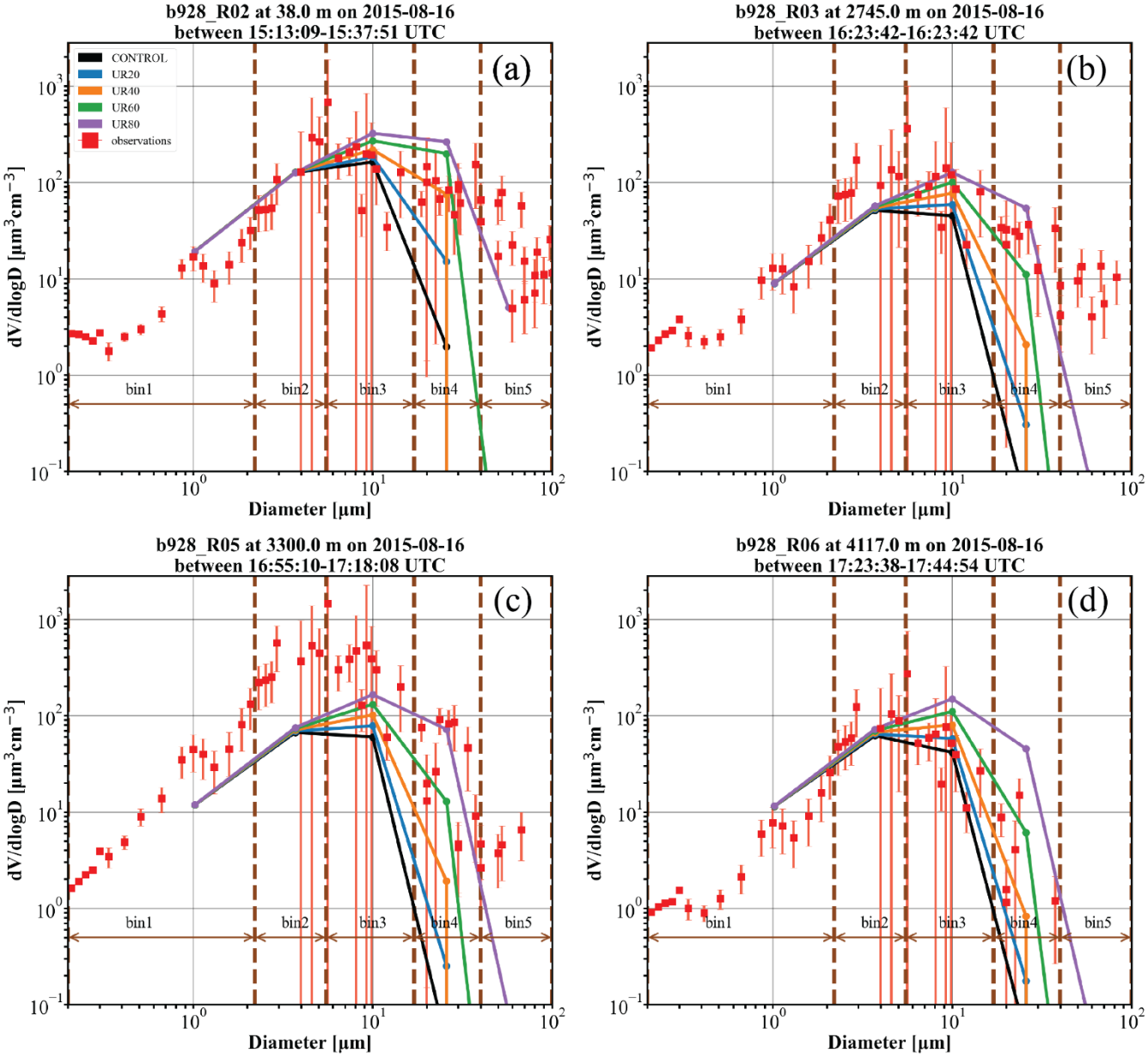

Figure 8: Modelled and observed dust PSD of flight b928, for straight-level-runs (a) R02, (b) R03, (c) R05, and (d) R06. The in situ observations are shown with red squares (along with uncertainties), and the modelled PSDs with lines, for the CONTROL run (black), UR20 (blue), UR40 (orange), UR60 (green), and UR80 (purple). The brown vertical lines indicate the limits of the model size bins. The modelled PSD are collocated in space and time with the corresponding observations.

https://doi.org/10.5194/acp-2022-94
Preprint. Discussion started: 7 April 2022
© Author(s) 2022. CC BY 4.0 License.

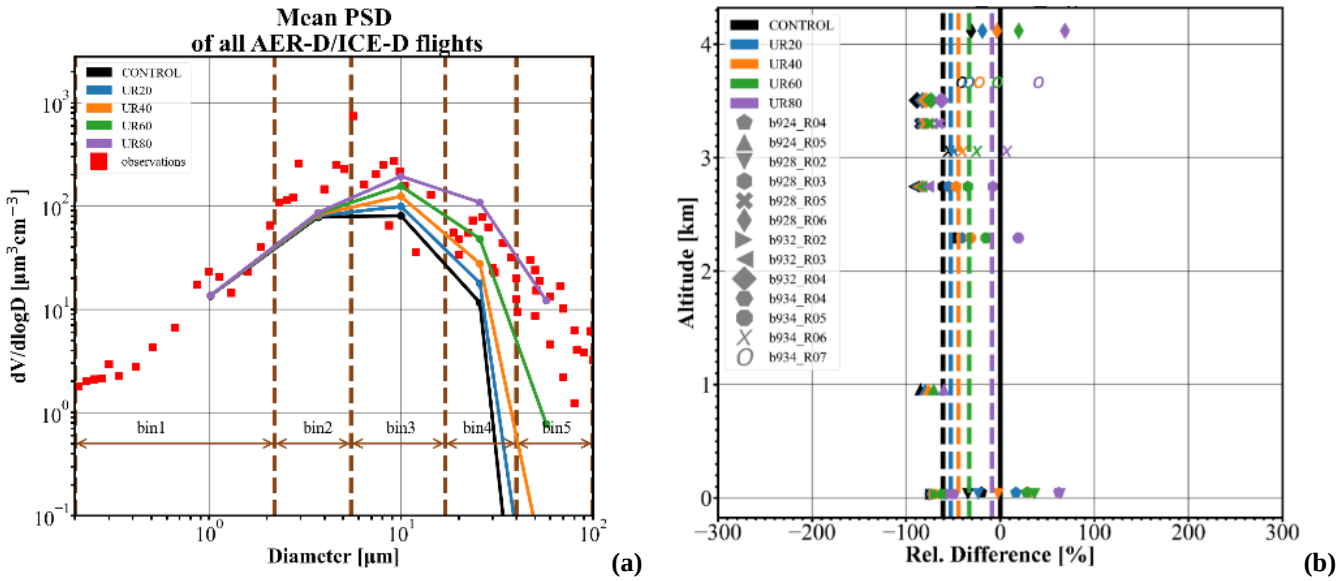

Figure 9: (a) Mean PSD of AER-D/ICE-D campaign. The observations are shown with red squares, whereas the simulations are shown with solid lines for the CONTROL run (black), UR20 (blue), UR40 (orange), UR60 (green), and UR80 (purple). (b) The relative difference between the observations and the model simulations of the total volume of dust particles, at different altitudes. The observations from different flight segments (i.e., b924_R04, b924_R05, b928_R03, b928_R05, b928_R06, b932_R02, b932_R03, b932_R04, b934_R04, b934_R05, b934_R06, and b934_R07) are denoted with different markers. The average relative difference of the observations and the simulations are denoted with dashed lines, for the CONTROL run (black), UR20 (blue), UR40 (orange), UR60 (green), and UR80 (purple).

https://doi.org/10.5194/acp-2022-94
Preprint. Discussion started: 7 April 2022
© Author(s) 2022. CC BY 4.0 License.

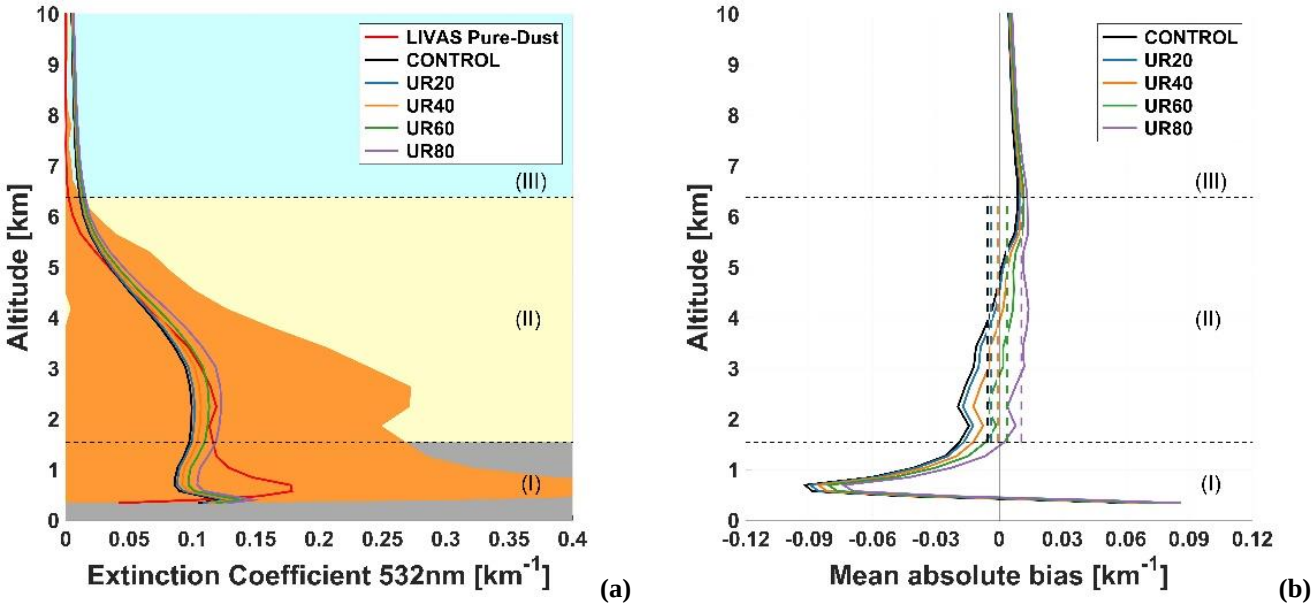

Figure 10: (a) Profile of the mean extinction coefficient at 532 nm, by LIVAS pure-dust product (black line), and profiles of the mean extinction coefficient at 532 nm simulated from the different experiments of Table 3 (CONTROL, UR20/40/60/80). The orange shading indicates the standard deviation of the LIVAS pure-dust product (b) The mean absolute biases between the LIVAS profile and the simulated profiles from the different experiments, in the domain of interest, between 05/08/2015 and 25/08/2015.

Table 1 Size ranges and properties of model size bins in the default WRF-GOCART-AFWA scheme

WRF-GOCART-AFWA					
Bins	**1**	**2**	**3**	**4**	**5**
$D_{lo} - D_u$(μm)	0.2-2.0	2.0-3.6	3.6-6.0	6.0-12.0	12.0-20.0
D_{eff} (μm)	1.46	2.8	4.8	9.0	16.0
ρ_p (g cm^{-3})	2.5	2.65	2.65	2.65	2.65

WRF-L					
Bins	**1**	**2**	**3**	**4**	**5**
$D_{lo} - D_u$(μm)	0.2-2.2	2.2-5.5	5.5-17.0	17.0-40.0	40.0-100.0
D_{eff} (μm)	1.02	3.7	10.0	25.8	57.2
ρ_p (g cm^{-3})	2.5	2.65	2.65	2.65	2.65

https://doi.org/10.5194/acp-2022-94
Preprint. Discussion started: 7 April 2022
© Author(s) 2022. CC BY 4.0 License.

Table 2 Configuration parameters of the WRF-L runs

Parameterization	Scheme	Parameterization	Scheme
Surface Model	Noah (Chen and Dudhia, 2001)	sf_surface_physics	2
Surface Layer	MM5 (Jiménez and Dudhia, 2012)	sf_sfclay_physics	2
Radiation (SW and LW)	RRTMG (Iacono et al., 2008)	ra_sw(lw)_physics	4
Microphysics	Morrison 2-moment (Morrison et al., 2005)	mp_physics	10
Cumulus	Grell-3 (Grell and Dévényi, 2002)	cu_physics	5
Boundary Layer	MYNN 2.5 (Nakanishi and Niino, 2006)	bl_pbl_physics	5
Chemistry	GOCART simple (Ginoux et al., 2001; LeGrand et al., 2019)	chem_opt	300
Dust Scheme	AFWA (LeGrand et al., 2019)	dust_opt	3

Table 3 Experimental runs that performed in this study

Experiment	Code
CONTROL	WRF-L
UR20	WRF-L with reduced settling velocities by 20% of their settling velocity
UR40	WRF-L with reduced settling velocities by 40% of their settling velocity
UR60	WRF-L with reduced settling velocities by 60% of their settling velocity
UR80	WRF-L with reduced settling velocities by 80% of their settling velocity